XMM-Newton study of the two-dimensional structure of the REFLEX-DXL galaxy clusters.

Alexis Finoguenov, Hans Böhringer, Yu-Ying Zhang

Max-Planck-Institut für extraterrestrische Physik, Giessenbachstraße, 85748 Garching, Germany

Abstract. We carry out a two-dimensional study of temperature, entropy and pressure distributions in a nearly volume-limited subsample of REFLEX clusters at redshift 0.3, the REFLEX-DXL. We use the observations gained by XMM-Newton, which cover the central $1 - 2 \times r_{500}$. We define the substructure in both entropy and pressure as a deviation from the mean profile of the sample. The non-parametric locally weighted regression suggests a broken power law approximation to the entropy profile with inner and outer slopes of 0.78 and 0.52, respectively, and a break at $0.5r_{500}$. The characterization of the pressure profile is more complex, requiring three power laws, with slopes -0.64 at $r < 0.3r_{500}$, -2.47 at $r > 0.5r_{500}$ and a slope of -1.50 in between. An analysis of the substructure in the pressure and entropy maps reveals somewhat larger fluctuations around the mean pressure profile compared to the entropy. Typically, pressure fluctuations are found on the 30% level, while the entropy fluctuations are at the 20% level (r.m.s.). We compare the cumulative distribution of the substructure level in the REFLEX-DXL sample with the results of numerical simulation and by means of KS test show that they are in agreement. A discussion of the origin of the substructure is provided on individual cluster basis.

Key words. Cosmology: observations — Galaxies: clusters: general

1. Introduction

Use of clusters of galaxies for cosmological tests in undergoing and future surveys rely on the understanding of the cluster physics. A number of observational and theoretical work has been devoted to studying the effects of non-gravitational heating in explaining the observed scaling of clusters with mass (see Voit 2004 for a review). Another long recognized issue consists in the effect of merging on the appearance of clusters (e.g. Randall et al. 2002; Rowley et al. 2004). It is widely accepted that the later effect dominates the appearance of the most massive clusters, where it also could be more pronounced, due to dependence of the accretion history of clusters on their mass. Thus, a study of the dynamical state of a representative sample of massive clusters appears to be well grounded. In this paper we explore the structure of individual clusters from a volume-limited sample of most massive clusters at a redshift of 0.3 to provide an in-depth coverage of the properties that define both the X-ray luminosity as well as the thermal Sunyaev-Zel'dovich effect (SZE) of clusters.

1.1. The REFLEX-DXL sample

The REFLEX-DXL galaxy cluster sample, comprising **d**istant **X**-ray **l**uminous objects within REFLEX, was constructed from the REFLEX galaxy cluster survey covering the ROSAT detected galaxy clusters above a flux limit of $3 \cdot 10^{-12}$ erg s^{-1} cm^{-2} in the 0.1 to 2.4 keV band in an 4.24 ster region of

the southern sky (see Böhringer et al. 2001 for details). The REFLEX-DXL clusters form a nearly volume limited subset of REFLEX in the redshift range 0.27 to 0.31 including 13 members plus a fourteenth cluster which was previously assigned to the sample but had to be excluded after a revision of the optically determined redshift. We have included this cluster here since it nicely fits into the homogeneous observational data properties of the REFLEX-DXL sample. All clusters exceed a luminosity of 10^{45} h_{50}^{-1} erg s^{-1} in the ROSAT band (0.1 to 2.4 keV). For five of the clusters the XMM observations were affected by strong proton flares. Their re-observation, which will be reported elsewhere, have provided us with good results except for one cluster, RXCJ2011–5725. One of the clusters included in the present study, RXCJ0658–5557, was a verification phase target with a significantly longer nominal observing time. Further properties of the REFLEX-DXL clusters are described in Zhang et al. (2004) and Böhringer et al. (2005, in prep.).

In Table 1 we summarize the properties of the clusters used in this study. Col. (1) gives the RXCJ designation of the source, (2–4) optical redshift, corresponding luminosity distance, and the conversion factor from apparent angular to physical scale (calculated for $\Omega_M = 1 - \Omega_\Lambda = 0.3$, and a Hubble constant of 70 km sec^{-1} Mpc^{-1}). Col. (5) gives the measured position of the cluster center, used in the analysis of cluster structure, (6) is the mean temperature T_w from Table 4 of Zhang et al. (2004), derived using the $0.5' < r < 4'$ region and the energy band $1 - 10$ keV. For the bullet cluster (RXCJ0658–5557), we

use the 0.4–10 keV band and remove the soft excess by an additional spectral component, for the reasons explained in detail below. (7) is r_{500} used for the scaling plots (an estimated radius encompassing the density equal to $500\rho_{crit}$), (8) lists the other names of the clusters.

The calculation of r_{500} is following $r_{500} = 0.45\mathrm{Mpc} \times \sqrt{kT_w/\mathrm{keV}}h_{70}^{-1}h(z)^{-1}$, where the scaling in Finoguenov et al. (2001) for h_{50} ($r_{500} \approx 0.63\mathrm{Mpc}\sqrt{kT/\mathrm{keV}}$) is translated into our assumption for $h_{70} = 1$. We use $h(z) = (\Omega_M(1+z)^3 + \Omega_\Lambda)^{1/2}$, suitable for our choice of the cosmological model. In Finoguenov et al. (2001) it has been demonstrated that the cosmological corrections are negligible in deriving the scaling for r_{500} in their sample of local clusters. These corrections are, however important for REFLEX-DXL.

The suggested modified entropy scaling reads $S \sim T_w^{0.65 \sim 2/3}h(z)^{-4/3}$ (Ponman et al. 2003). In the analysis of clusters, we will also present scaled pressure plots. As entropy, $Tn^{-2/3}$, scales as $T_w^{2/3}$, the density scales as $T_w^{1/2}$ and the pressure $Tn \sim T_w^{3/2}$. Finally the correction for the evolution of the critical density is $h(z)^2$. Throughout the paper we will use the corrections by $T_{10} = \frac{T_w}{10\mathrm{keV}}$. For the temperature profiles, however, we simply correct for the T_w to match other studies.

2. Analysis

The main goal of the primary data reduction is to produce soft and hard images based on merging the data obtained by all EPIC detectors. Initial steps of the data reduction include the XMMSAS event processing, and light curve screening, which is similar to the approach adopted by other groups (e.g. De Luca & Molendi 2003). The background subtraction has been described in Zhang et al. (2004).

With these screened photon event files we produced MOS and pn images of the individual observations in the energy bands from 0.5 to 2.0 and 2.0 to 7.5 keV with more details available in Briel et al. (2004).

The broad-band images can be used for making visible intensity structures, and variations of the temperature of the X-ray emitting plasma by producing hardness-ratio maps, which can be uniquely translated into a plasma temperature distributions. In addition, one can produce pressure and entropy maps of the plasma by combining the surface brightness map and the hardness ratio map. Useful hardness ratio maps can only be produced from smoothed surface brightness maps. There exists a variety of different smoothing procedures like top-hat smoothing, Gaussian smoothing or adaptive smoothing (e.g. Churazov et al. 1999). We applied the wavelet decomposition method, which is described in detail by Vikhlinin et al. (1998). The advantage of using wavelets consists in background removal by spatial filtering and a control over the statistical significance of the detected structures. Complications arise due to splitting the image into discrete scales, which we overcome by additional smoothing applied before producing the hardness ratio map. The use of wavelets provides us with a decent method to identify the regions susceptible to temperature variations. Another important feature is the high spatial resolution achieved in detecting the structure, as wavelets do not smear the data.

For every cluster, we show the results of the broad-band image investigation, an image in the 0.5–2 keV energy band, the hardness of the emission, deduced from the ratio of the wavelet-reconstructed images in the 0.5–2 and 2–7.5 keV bands, as well as the projected pressure and entropy maps, constructed using the wavelet-smoothed surface-brightness map in the 0.5–2 keV energy range as an indicator of the electron density squared and the hardness ratio map as temperature distribution, and using the definitions of the pressure $P \sim T \times \sqrt{I}$ and of the entropy $S \sim T/\sqrt[3]{I}$. In addition to visualizing the temperature distribution through hardness ratios we also determined the local temperatures spectroscopically.

The spectral analysis was carried out using only the pn data. Background subtraction here is more demanding and based on the XMM observations of the Chandra Deep Field South, as described in Zhang et al. (2004). We have selected the 0.4–7.9 keV band for the analysis of all the clusters and added a soft ($kT \sim 0.2keV$) spectral component to remove any soft excess. For the most affected system, the bullet cluster (RXCJ0658–5557), we find a good agreement between the mean temperatures using this method (12.3 ± 0.3) and the 1–10 keV band (11.8 ± 0.3).

In the spectral analysis we produced two masks per cluster defining the spectral extraction region, one to confirm the temperature structure, combined with the image, the other – to confirm pressure and entropy structure. We combine the regions so that counting statistics are not the limiting factor in our derivation of the cluster properties. We use the wavelet-based maps to identify regions with similar X-ray colors and intensity levels. To generate the mask file for use in the subsequent spectral analysis, we sample the changes in the intensity and hardness ratio at the precision allowed by the statistics of the data. We then examine each of the isolated regions with approximately equal color and intensity, imposing an additional criterion that the regions should be larger than the PSF width (15″) and contain more than 500 counts in the background corrected pn image. When sampling the pressure and entropy structure, the region selection should be fine to achieve a nearly equal temperature within the region, as the X-ray data is only sensitive to pressure and entropy by measuring the temperature and normalization of the spectra. So, we used finer region selection with a reduced threshold on a number of counts (300), resulting in a higher number of regions at expense of larger uncertainty in the parameter determination. So, in the paper we tabulate mostly the confirmation of the temperature structure, with exception of RXCJ0232.2–4420 and the bullet cluster, where the other mask was more useful.

For every cluster we provide a table, containing the measured values with their ±1σ errors for one parameter of interest. As all these tables are similar, we give a single description for all here. Col. (1) labels the region according to region selection shown in the accompanied figure, column (2) lists the temperature in keV. Derived quantities, that use an estimate of the projected length, as described below are reported in cols. (3–6). These are electron density, entropy, pressure, and the (local) gas mass. Cols. 7–8 report the minimal (r_{min}) and maximal (r_{max}) radii of the extraction area, col. (9) provides remarks on the region.

Table 1.   Scaling assumptions for the analyzed clusters.

RXCJ name	z	D_l Mpc	plate scale kpc/″	cluster center R.A., Decl. FK5 (Eq.J2000)	kT_{ew} keV	r_{500} Mpc	other names
0014.3–3022	0.3066	933	271	00:14:19.288 –30:23:07.41	8.3 ± 0.4	1.11	A2744, AC118
0043.4–2037	0.2924	903	263	00:43:24.446 –20:37:30.72	6.8 ± 0.4	1.01	A2813
0232.2–4420	0.2836	884	257	02:32:18.561 –44:20:48.40	7.6 ± 0.4	1.07	
0307.0–2840	0.2578	825	240	03:07:02.084 –28:40:00.21	6.6 ± 0.3	1.01	A3088
0528.9–3927	0.2839	885	257	05:28:52.731 –39:28:24.82	7.7 ± 0.6	1.08	
0532.9–3701	0.2747	864	251	05:32:56.043 –37:01:33.52	7.8 ± 0.6	1.09	
0658–5557	0.2965	912	265	06:58:31.453 –55:56:16.74	12.3 ± 0.3	1.37	1ES0657-558
1131.9–1955	0.3075	935	272	11:31:55.742 –19:55:42.82	7.4 ± 0.5	1.05	A1300
2337.6+0016	0.2779	871	253	23:37:38.323 +00:16:05.07	7.5 ± 0.4	1.07	A2631

For this detailed analysis we also perform an estimate of the projection length of each analyzed region to obtain actual gas properties at these locations, as described at length in Henry et al. (2004) and Mahdavi et al. (2005). To avoid the importance of the projection effects, we discard the regions having a ratio of the minimal to the maximal radii of values exceeding 0.8.

3. Results

The statistics achieved in the observation of the REFLEX-DXL clusters allows us only to recognize the strongest fluctuations in either temperature, entropy, or pressure. In the presentation of the results we indicate the features seen in the hardness ratio based maps and discuss how much it is possible to confirm them through a direct spectroscopic analysis. In selecting the regions according to their properties or according to their statistics, we implicitly perform an adaptive filtering of the signal. It is therefore important to characterize the spatial frequencies sampled in the analysis, which is also a way to characterize the analysis carried out and the cluster spatial scales sampled. In Fig.1 we present such an analysis, where it becomes clear that the choice of the regions corresponds to a grid in cylindrical coordinates, sampling the azimuthal angle with typically 3 sectors on radial scales from 0.1 to 1 Mpc.

Since there is a discussion on the reliability of the temperature determination, we have provided a plot for each cluster, where a comparison to the average cluster temperature profile of Vikhlinin et al. (2005) is presented. One can see in each case that there is a good agreement in the results. We also point out that a few clusters where we probed the region outside r_{500}, reveal strong asymmetries indicating accretion from a filament. It may be that the presence or removal of such zones could be the underlying reason for some of the reported disagreement in temperature profiles.

We define a cool core of a cluster or its debris as the gas with entropy significantly below 200–300 keV cm^2, which according to Voit & Bryan (2001) could cool in a Hubble time. As local examples of cool cores have entropies lower than 100 keV cm^2, we have used the later criterion for the cooling core identification.
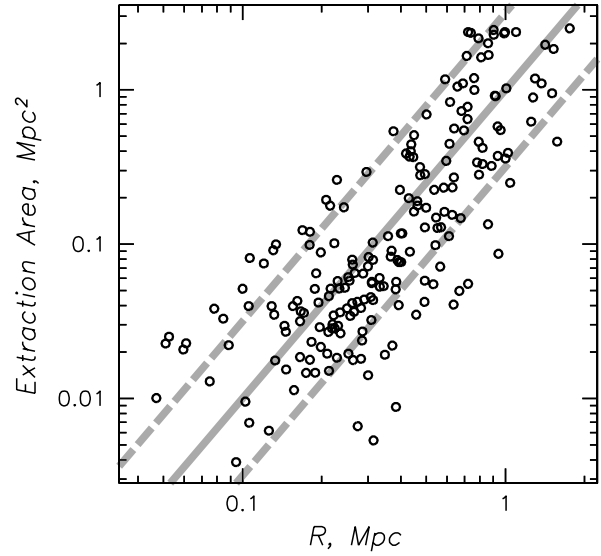

Fig. 1. Characterization of the ability of the current masking technique to reveal spatial variations in the spectral properties of gas as a function of clustercentric distance (window function). The points indicate an extraction area in Mpc^2 as a function of radius of the zone, calculated as $(r_{min} + r_{max})/2$. The grey lines indicate a quadratic dependence of the area on the radius. The data is in remarkably good agreement with these curves, indicating that the sampling corresponds roughly to a grid in cylindrical coordinates. The upper dashed line correspond to the case of no sampling on azimuth, solid line – having 3 regions and low dashed line – 10 to sample the azimuthal scale.

Before proceeding with the description of individual systems, we summarize the results by presenting the fits to the entropy and pressure profiles. To define the shape of the entropy and pressure profiles, we applied the non-parametric locally weighted regression, following Sanderson et al. (2005 and references therein). This analysis results in the non-parametric curve, which we approximate below with power laws. Our analysis illustrated in Fig.2 suggests a broken power law approximation to the entropy profile with an inner and an outer slopes of 0.78 and 0.52, respectively, and a break at $0.5r_{500}$.

The amplitude of fluctuations around the best exceeds the effect of the statistics and is a measure of the important of substructure, as discussed below. The average level of fluctuations, which is 15% (20%) in the case of entropy (pressure), could be taken as the accuracy to which the approximation to the entropy distribution could be determined. The entropy profiles with exclusion of the substructure has been analyzed in Zhang et al. (2005), yielding a steeper index of 0.95. The characterization of the pressure profile is more complex, requiring three power laws, with slopes -0.64 at $r < 0.3r_{500}$, -2.47 at $r > 0.5r_{500}$ and a slope of -1.50 in between. For completeness, we present in Tab.2 a standard approach of using the orthogonal regression and assuming a power law shape to approximate the shape of the entropy and pressure profiles. We present the results obtained using different masks and also combine the clusters with and without the rescaling, described above. As could be easily seen from Tab.3, this approach results in a much larger amplitude of the residuals, even taking into account that the power law shape was fitted separately for each cluster, while in the non-parametric approach, one shape is used to approximate all clusters.

Table 2. Results of the orthogonal regression analysis of entropy and pressure profiles.

Name RXCJ	$S(0.2r_{500})$ keV cm^2	S slope	$P(0.2r_{500})$ 10^{-11} ergs cm^{-3}	P slope
0014.3–3022	373 ± 21	0.30 ± 0.12	7.8 ± 1.1	-1.70 ± 0.34
	352 ± 29	0.40 ± 0.13	13.9 ± 1.6	-2.28 ± 0.23
0043.4–2037	416 ± 32	0.05 ± 0.30	5.2 ± 0.7	-1.69 ± 0.21
	287 ± 17	0.61 ± 0.16	5.1 ± 0.3	-1.92 ± 0.12
0232.2–4420	280 ± 18	0.60 ± 0.19	4.3 ± 0.4	-1.35 ± 0.16
	236 ± 46	0.50 ± 0.62	4.2 ± 0.6	-0.91 ± 0.40
0307.0–2840	222 ± 7	0.91 ± 0.12	2.8 ± 0.2	-1.41 ± 0.12
	243 ± 3	0.93 ± 0.06	3.3 ± 0.2	-1.35 ± 0.20
0528.9–3927	173 ± 17	0.86 ± 0.21	4.4 ± 0.4	-1.55 ± 0.20
	124 ± 24	1.10 ± 0.36	4.9 ± 0.5	-1.64 ± 0.43
1131.9–1955	279 ± 22	0.73 ± 0.24	6.2 ± 0.7	-1.72 ± 0.24
	238 ± 10	0.79 ± 0.18	5.9 ± 0.5	-1.83 ± 0.21
2337.6+0016	324 ± 20	0.80 ± 0.15	3.9 ± 0.2	-1.20 ± 0.15
	354 ± 35	0.63 ± 0.30	4.3 ± 0.7	-1.39 ± 0.48
0532.9–3701	435 ± 33	0.11 ± 0.10	2.8 ± 0.7	-0.64 ± 0.52
	296 ± 13	0.21 ± 0.23	6.8 ± 0.3	-2.18 ± 0.13
0658–5557	382 ± 15	0.86 ± 0.11	8.3 ± 0.5	-1.34 ± 0.21
	379 ± 16	0.94 ± 0.09	7.5 ± 0.4	-1.62 ± 0.17
all	290 ± 8	0.62 ± 0.09	5.4 ± 0.2	-1.54 ± 0.10
$r > 0.25r_{500}$	381 ± 53	0.38 ± 0.27	11.4 ± 1.0	-2.15 ± 0.17
$r < 0.25r_{500}$	388 ± 31	1.33 ± 0.37	6.0 ± 0.5	-0.77 ± 0.44
T&z-corrected	452 ± 11	0.64 ± 0.08	6.8 ± 0.2	-1.43 ± 0.10
$r > 0.25r_{500}$	570 ± 72	0.44 ± 0.24	11.5 ± 1.1	-1.88 ± 0.18
$r < 0.25r_{500}$	509 ± 31	1.10 ± 0.27	5.8 ± 0.5	-1.09 ± 0.45

One of the most important results is an observation of a flattening in the entropy profile at outer radii in DXL clusters, changing from 0.78 within the $0.5r_{500}$ to 0.54 outside. As the sample consists of the most massive clusters in the Universe, we believe that the explanation of the observed trend should be searched in the details of the accretion. As summarized in Voit (2004), the index of the entropy profile is driven by the effects of mass growth as well as evolution of the virial den-
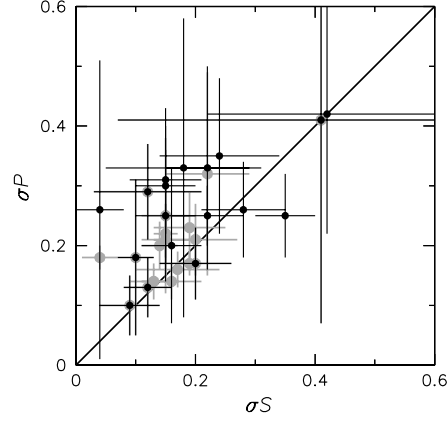

Fig. 3. Correlation in the dispersion of entropy and pressure. Grey points indicate measurements within $0.4r_{500}$ and solid points – in full range of radii. The solid line show the one-to-one ratio between the entropy and pressure.

sity. Under the assumption of a smooth accretion, the entropy grows with radius as $S \sim M_{gas}^{1-4/3}$ (Voit 2004). With a canonical cluster characteristic of the surface brightness profile, $\beta = 2/3$, $M_{gas} \sim r$, where M_{gas} is enclosed gas mass. However, as gas mass fraction tends to level off at high radii, the cumulative gas mass starts to follow the mass of the dark matter and so $M_{gas} \sim r^{0.5}$. A similar flattening in the entropy distribution is then expected and is observed in our data at $r \geq 0.4r_{500}$. If this indeed is the explanation to our data, one would not necessarily expect the same trend to be observed in low-mass clusters, where the baryon fraction is growing with the radius even at r_{500}.

In addition to the provided explanation, we would like to mention that with faster mass growth of the cluster (as during a major merger), the entropy profile should become flatter (Voit 2004). Yet another effect, associated with the survival of the low entropy gas during the merger (Motl et al. 2004), reduces the increase in the entropy associated with the mass growth and should effectively lead to flatter entropy profiles, however, the full details should be obtained from simulations.

Once the general behavior of the entropy and pressure is found, we studied the amplitude of the deviations from the average profile, allowing for the change in the normalization and compared that with the statistical errors in Table 4.

In Fig.3 we study the scatter in the entropy and pressure, reported in Table 4. The dispersion and normalization of the profile are calculated weighting the points by the area of the corresponding region. The renormalization is needed to remove a possible bias due to assumption of a mean temperature in rescaling the profiles. We note that the spread of values for the normalization is larger for the pressure, where also the sensitivity to the assumed weighted temperature is larger. There is also no clear correlation between the r.m.s. values and the normalization in either entropy or pressure. The figure shows that the fluctuations in the entropy and pressure are correlated in the magnitude, with the relation favoring slightly higher pressure fluctuations as compared to the entropy, but certainly not following the prescription for the shock heating, which at the

Table 3. Entropy and pressure fluctuations around the power law approximation, reported in Tab.2.

Name RXCJ	σS	σP	σS	σP	σS	σP
	$r < 0.3r_{500}$		$r > 0.2r_{500}$		from individual fits	
0014.3–3022	0.58 ± 0.07	0.62 ± 0.07	0.26 ± 0.07	0.45 ± 0.05	0.26 ± 0.07	0.75 ± 0.08
	0.47 ± 0.07	0.74 ± 0.06	0.10 ± 0.09	0.47 ± 0.07	0.12 ± 0.05	1.05 ± 0.08
0043.4–2037	0.49 ± 0.06	0.64 ± 0.11	0.44 ± 0.12	0.44 ± 0.20	0.47 ± 0.14	1.04 ± 0.14
	0.44 ± 0.11	0.64 ± 0.09	0.08 ± 0.08	0.11 ± 0.08	3.61 ± 0.25	0.91 ± 0.42
0232.2–4420	0.34 ± 0.16	0.52 ± 0.06	0.46 ± 0.21	0.47 ± 0.16	0.40 ± 0.20	0.58 ± 0.05
	0.21 ± 0.04	0.62 ± 0.15	0.25 ± 0.05	0.41 ± 0.16	0.25 ± 0.05	1.00 ± 0.11
0307.0–2840	0.29 ± 0.06	0.28 ± 0.05	0.26 ± 0.07	0.24 ± 0.07	0.28 ± 0.06	0.25 ± 0.06
	0.10 ± 0.03	0.45 ± 0.05	0.16 ± 0.04	0.17 ± 0.04	0.04 ± 0.02	0.48 ± 0.05
0528.9–3927	0.28 ± 0.12	0.46 ± 0.08	0.22 ± 0.11	0.36 ± 0.13	0.33 ± 0.11	0.39 ± 0.10
	0.16 ± 0.06	0.67 ± 0.08	0.14 ± 0.10	0.40 ± 0.09	0.17 ± 0.06	0.53 ± 0.09
1131.9–1955	0.42 ± 0.05	0.45 ± 0.07	0.29 ± 0.05	0.32 ± 0.06	0.37 ± 0.04	0.50 ± 0.07
	0.57 ± 0.05	0.74 ± 0.08	0.29 ± 0.07	0.44 ± 0.08	0.78 ± 0.05	0.81 ± 0.07
2337.6+0016	0.31 ± 0.08	0.44 ± 0.18	0.26 ± 0.08	0.38 ± 0.20	0.23 ± 0.09	0.49 ± 0.16
	0.22 ± 0.05	0.41 ± 0.11	0.15 ± 0.05	0.23 ± 0.16	0.15 ± 0.05	0.54 ± 0.09
0532.9–3701	0.58 ± 0.34	0.75 ± 0.52	0.43 ± 0.33	0.44 ± 0.30	0.41 ± 0.31	1.41 ± 0.72
	0.52 ± 0.05	0.73 ± 0.09	0.35 ± 0.06	0.28 ± 0.07	0.36 ± 0.05	0.62 ± 0.08
0658–5557	0.27 ± 0.05	0.54 ± 0.07	0.25 ± 0.07	0.40 ± 0.11	0.19 ± 0.07	0.57 ± 0.07
	0.18 ± 0.04	0.62 ± 0.06	0.21 ± 0.06	0.25 ± 0.04	0.13 ± 0.04	0.55 ± 0.05
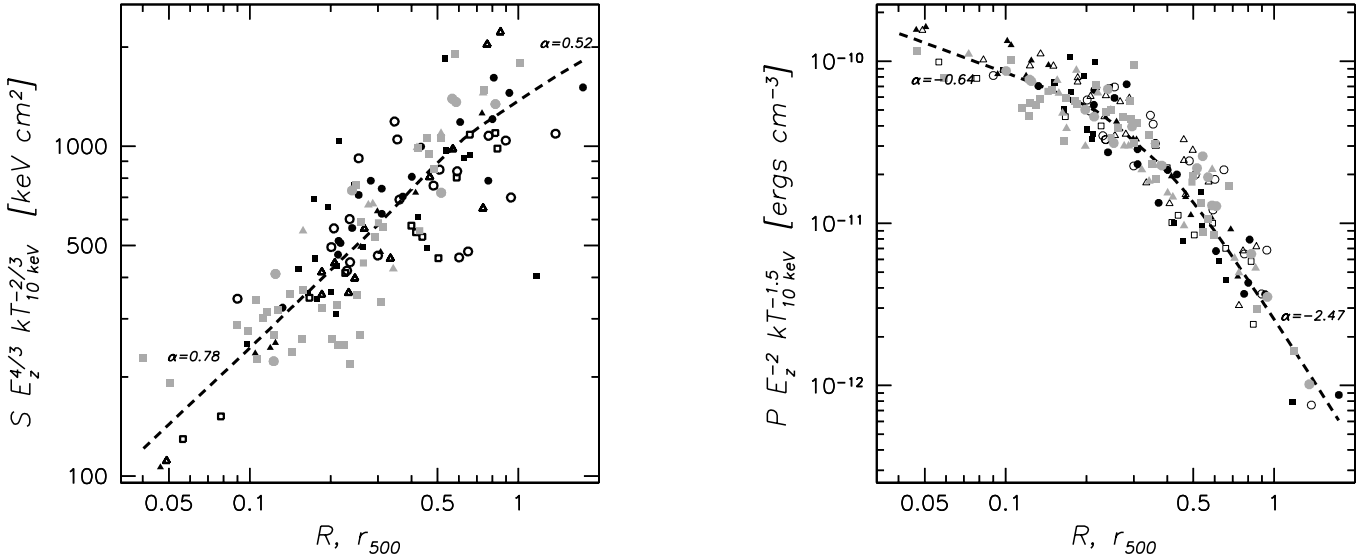
Fig. 2. Comparison between the entropy and pressure of the sample and the analytical approximation, used to study the dispersion. The entropy and pressure points corresponding to the same cluster are shown using the same symbol. The dashed line show the results of the fit using the non-parametric locally weighted regression method.

observed amplitudes predicts fluctuations only in the pressure and very little in the entropy. This picture and a quantitative analysis below is very similar to the results of Finoguenov et al. (2005), who analyzed a set of cosmological simulations of clusters. Apparently, azimuthal distortions, related to gas and dark matter displacements during the merger and post relaxation supersede the distortions associated with the shock heating. The later accounts for about 15% and its clear separation could be better revealed in the future by comparison of pressure maps derived at X-rays and thermal SZE observations.

In Fig.4 we summarize the fluctuation analysis and compare it with the distribution for the cluster sample obtained in the cosmological simulations (Finoguenov et al. 2005) sampling a similar range of radii. Taking the comparison between

the model and the results obtained with the mask sampling pressure and entropy, we conclude that the clusters show a similar degree of fluctuations and the probability of this to be randomly drawn from the same distribution, calculated using the KS-test, is 60% and 80% for the pressure and entropy, respectively. We combined the results of the two masks in the test.

3.1. RXCJ0014.3–3022

The cluster consists of two clumps. The large-scale emission is centered on one of the peaks, that is therefore taken for the center of the main cluster and its position is listed in Tab.1. In order to tabulate the basic properties of the cluster we extracted the spectra from zones that according to the hardness ratio have

Table 4. Entropy and pressure fluctuations around the mean sample trend. The results of the spectral analysis using two different masks are shown. The I-T is the mask based on cross-sections of the isothermal and isodensity regions. The S-P is the mask based on the cross-sections of the isentropic and isobaric regions.

| Name	σS	σP	σS	σP
RXCJ	I-T-mask		S-P-mask	
0014.3–3022	0.22 ± 0.06	0.25 ± 0.05	0.15 ± 0.06	0.31 ± 0.09
0043.4–2037	0.18 ± 0.13	0.33 ± 0.25	0.04 ± 0.04	0.26 ± 0.25
0232.2–4420	0.42 ± 0.20	0.42 ± 0.20	0.15 ± 0.05	0.30 ± 0.13
0307.0–2840	0.20 ± 0.06	0.17 ± 0.06	0.09 ± 0.05	0.10 ± 0.05
0528.9–3927	0.16 ± 0.05	0.20 ± 0.13	0.12 ± 0.09	0.29 ± 0.08
1131.9–1955	0.12 ± 0.04	0.13 ± 0.05	0.28 ± 0.07	0.26 ± 0.08
2337.6+0016	0.22 ± 0.07	0.33 ± 0.17	0.10 ± 0.03	0.18 ± 0.13
0532.9–3701	0.41 ± 0.34	0.41 ± 0.34	0.35 ± 0.05	0.25 ± 0.07
0658–5557	0.24 ± 0.10	0.35 ± 0.13	0.15 ± 0.05	0.25 ± 0.11
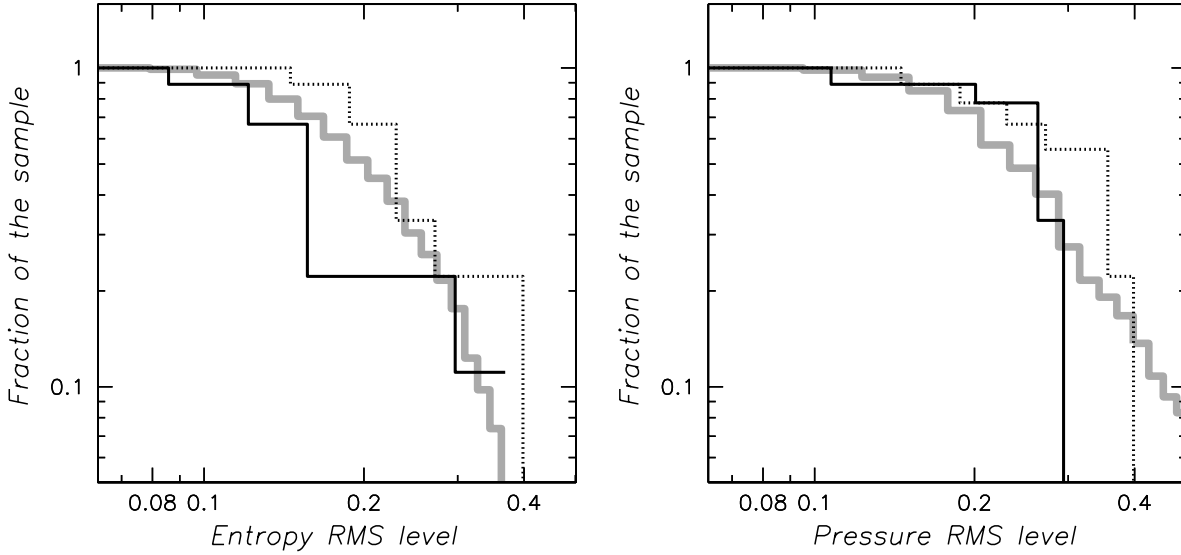
Fig. 4. Fraction of clusters with RMS of the entropy (left panel) and pressure (right panel) parameter greater than the x-axis value. Black lines denote the results for DXL cluster sample, obtained using two different masks (marked as solid and dotted lines), correspondingly sampling entropy/pressure and image/temperature. Grey line represents the results of a similar analysis performed on a sample of 208 modeled clusters (Finoguenov et al. 2005).

Table 5. Properties of main regions of RXCJ0014.3–3022.

N	kT	ρ_e	S	P, 10^{-12}	M_{gas}	r_{min}	r_{max}	Remarks
	keV	10^{-4} cm^{-3}	keV cm^2	ergs cm^{-3}	$10^{12} M_\odot$	Mpc	Mpc	
1	2.6 ± 0.7	1.9 ± 0.4	785 ± 242	0.8 ± 0.3	25.9 ± 5.9	0.92	2.14	main-3
2	12.5 ± 3.6	21.2 ± 2.3	754 ± 226	42.4 ± 13.2	2.7 ± 0.3	0.27	0.51	ridge S
3	8.7 ± 1.7	23.2 ± 1.6	495 ± 102	32.2 ± 6.8	3.4 ± 0.2	0.25	0.56	ridge N
4	4.7 ± 0.4	5.0 ± 0.2	748 ± 64	3.8 ± 0.3	58.8 ± 1.8	0.58	1.41	main-2
5	6.7 ± 0.3	11.7 ± 0.2	604 ± 29	12.5 ± 0.6	49.1 ± 0.7	0.25	1.07	main-1
6	9.2 ± 0.6	34.5 ± 0.6	405 ± 27	51.1 ± 3.4	14.9 ± 0.2	0.03	0.43	ridge
7	6.7 ± 0.7	33.3 ± 1.6	302 ± 32	35.9 ± 4.0	2.7 ± 0.1	0.13	0.38	disrupted core
8	6.0 ± 0.8	23.0 ± 1.6	345 ± 49	22.2 ± 3.3	3.2 ± 0.2	0.57	0.87	subcluster

the same temperature to within 1 keV. Table 5 contains three zones with temperatures exceeding 7 keV. These zones form a ridge passing between the two subclusters and surrounding the main cluster center. The elongated shape of the ridge suggests its origin in the interaction between the clusters. The temperature enhancement compared to region 5 is a factor of 1.4 ± 0.1, which corresponds to a Mach number of 1.4 ± 0.1. Although, higher temperatures are also observed, they are not statistically different from 9 keV. The pressure peak is not at the cluster center, but is within the ridge.

The temperature as well as the pressure of the subcluster (region 8) are similar to that of the disrupted core of the main cluster (region 7, as well as 5). Assuming that the mass scales with the central pressure as $M \sim P^{1.5}$, the initial mass ratio of
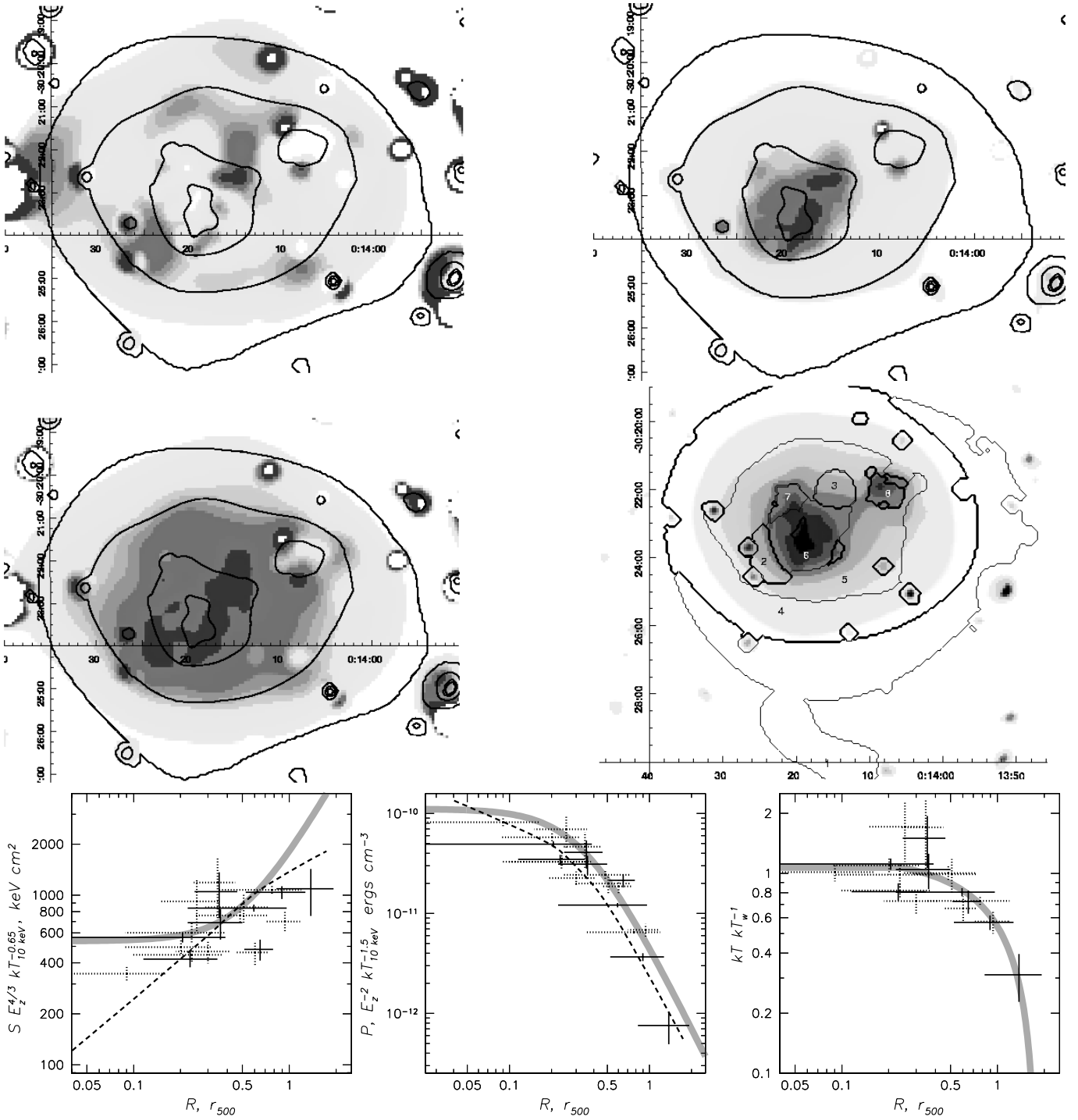
Fig. 5. RXCJ0014.3–3022. Top left: entropy map, top right: pressure map, middle left: temperature map, middle right surface brightness. Entropy, pressure and temperature maps are overlaid with the contours of equal surface brightness in the 0.5–2 keV band. The surface brightness image is overlaid with contours showing the spectral extraction regions with numbers corresponding to those in Table 5. Coordinate grids are shown for the epoch J2000. On the corresponding maps, zones of low entropy are shown in white, zones of higher pressure, temperature are shown in black. Lower left entropy profile, lower center: pressure profile, lower right: temperature profile. The solid crosses denotes the tabulated data and the dotted crosses show the rest of the results. The data is scaled for both the cluster mass, using the relation of Ponman et al. (2003) and evolution of the critical density with redshift. Dashed lines on both plots shows the best fit to the whole sample, described in the text. Grey lines show the results of the 1d analysis, using a beta-model and fits to the temperature profile from Zhang et al. (2005, in prep.). The grey line in the temperature panel is the universal temperature profile of Vikhlinin et al. (2005).

the two clusters is 1.7 ± 0.2. An expected final temperature of the cluster after the merger from the $M-T$ relation (Finoguenov et al. 2001) is 9.1 ± 0.5 keV, similar to the observed temperature of the ridge. This comparison suggests that the grown mass of the new cluster will be able to cope with the increased pressure of the gas.

In Fig.5 we also compare the derived entropies and pressures with the average trend for the DXL sample and further illustrate their ratio in Figs. 14-15. It can be seen that the entropy of the core region is higher by a factor of 1.3 ± 0.05. Low entropy clump is seen at the position of the second core. The pressure of the bridge appears to match well the adopted scaling temperature of 8.3 keV. The pressure of the main cluster at the distance of the subcluster (region 5) is by a factor of 1.5 ± 0.05 higher than the model, despite of a relatively low temperature of 6.7 keV.

The subcluster is characterized by higher pressure (best seen in the Table 5 and as deviation in the pressure profile) as well as lower entropy. This implies that the low entropy gas of the subcluster is retained within its own dark matter halo. This picture is different from the case of A3667 (Briel et al. 2003), where low entropy gas is displaced from the pressure peak. The subcluster in A2744 is a cool core, rather than a cold front. Our identification of the core of the main cluster is further confirmed by the entropy plot, as it lies on the prediction for the self-similar scaling. It is located 0.2 Mpc apart from the cluster center and may even present the still unperturbed part of an initially large cluster core extending to that radii.

In Fig.5 we also show the results produced by the standard analysis using the beta model (e.g. Jones & Forman 1984). We find an overall agreement between the two methods.

For many of the described features there is a qualitative agreement with Chandra results of Kempner & David (2004). Similar high temperature ridges have been claimed for A1644 (Reiprich et al. 2004) and A3921 (Belsole et al. 2005), yet none of them are found to dominate the pressure of the cluster, as in the case of A2744.

3.2. RXCJ0043.4–2037

If one judges from the image, this is one of the most relaxed clusters in the sample. The image has a single center, which is located at the center of the large-scale emission. However, there is an indication of small pressure and entropy distortions and the statistical analysis reveals that the fluctuations are quite large. The pressure shape follows essentially the temperature shape. Some small-scale fluctuations in the temperature map are still seen. The image is extended to the north-west.

The results of the spectral analysis are reported in Table 6 and shown in Fig.6. The most significant feature is the presence of a region with extremely low entropy, seen as dotted cross in the entropy profile in Fig.6 at the $0.7r_{500}$ distance to the center to the south. This gas is in pressure equilibrium with the cluster, leading to a suggestion that we observe the debris of accreted group. A comparison with simulations would be useful here to shed more light on the stage of this suggested disruption. Given the statistical uncertainty it is difficult to conclude on the origin

of the extent towards the north-west in the lowest levels of the X-ray surface brightness (region 5). Presumably, this extension, located outside of r_{500}, is due to an accretion of a filament.

3.3. RXCJ0232.2–4420

The hardness ratio map reveals a soft compact source in the center. In the image we see some elongation to the north. In the inner region the surface brightness distribution shows an indication of a triangular shape with one tip of the triangle pointing towards the north and the other to the west. As a result what we see is that there is colder material in the east compared to the west. The pressure map looks rather symmetric, but we have an asymmetric entropy structure. While a possible scenario could be a slow infall of the material from the north-east, the west part of the cluster appears to be systematically hotter as compared to the eastern side, which could be an indication of a strong shock.

The spectroscopic analysis is reported in Table 7 and Fig.7. The point-like source appears to be the low-entropy core of the cluster, with one of the lowest entropies (77 ± 4 keV cm^2) in our sample. The hot region on the west is characterized by both an enhancement in the pressure and entropy, yet of high statistical uncertainty. We attribute the appearance of this region to a forward shock of the Mach number of 3 ± 1. The low entropy gas in the north east (region 9) is confirmed in the spectral analysis. The behavior of the entropy in the outskirts of this cluster led us to a conclusion, supported by other clusters in this sample: the clusters in the advanced stage of interaction have systematically higher entropy at r_{500} compared to the average trend. We ascribe this result to the heating by the forward shock, induced during the merger.

3.4. RXCJ0307.0–2840

The cluster seems to be quite relaxed judging from the symmetric appearance of the image and the pressure map. The temperature map shows small amplitude fluctuations. According to the spectroscopic analysis, reported in Table 8 and shown in Fig.8, the cluster has a cool core, but otherwise exhibits no significant deviations from the modified scaling relation, bearing a slightly higher entropy and showing no fluctuations in the pressure profile. The 1d and 2d modeling agree well with each other.

3.5. RXCJ0528.9–3927

A strong soft point source near the center ($< 20\%$ of the flux) prevents us from a more detailed analysis of the central region. The pressure peak is distorted on small scales, while on large scales it appears quite relaxed. There is some entropy and temperature structure in the north-west.

The spectroscopic analysis reported in Table 9 and Fig.9 does not include the region 1, which is associated with the point-like source and reveals a clearly non-thermal spectrum. The suggested fluctuations in the north-west are confirmed to be a zone of lower entropy and also in general the entropy of
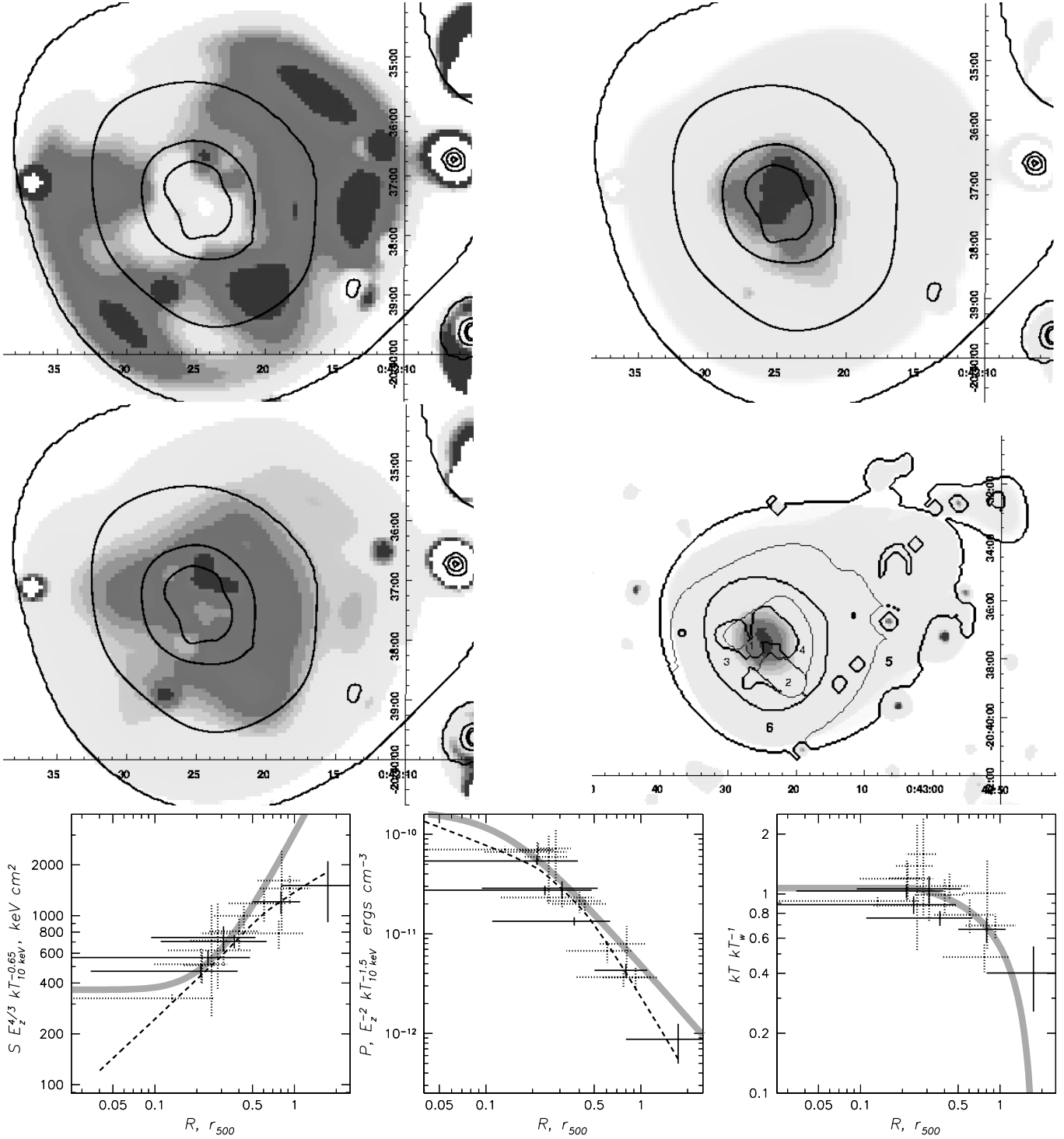
Fig. 6. RXCJ0043.4–2037. Figure caption is similar to that of Fig.5. The surface brightness image is overlaid with contours showing the spectral extraction regions with numbers corresponding to those in Table 6.

this cluster is lower at almost every radii, compared to the general trend.

3.6. RXCJ0532.9–3701

This cluster shows one of the most symmetrical images in the sample. It has a low-entropy core, but not low enough for a cool core. The pressure map is also quite symmetric. In the intensity we see a slightly boxy structure and associated with it a clover leaf structure in the entropy. On large scales the temperature is anti-correlated to the density in azimuthal direction, resulting in a constant pressure.

The spectroscopic analysis is reported in Table 10 and Fig.10. The cluster exhibits a low-entropy infalling zone to the east (region 8). Its entropy is 286 ± 65 keV cm^2, which is lower compared to the 665 ± 55 keV cm^2 value for the preceding zone

Table 6. Properties of main regions of RXCJ0043.4–2037.

N	kT keV	ρ_e 10^{-4} cm^{-3}	S keV cm^2	P, 10^{-12} ergs cm^{-3}	$M_{\rm gas}$ $10^{12} M_\odot$	$r_{\min}$ Mpc	$r_{\max}$ Mpc	Remarks
1	7.0 ± 0.6	36.0 ± 0.8	300 ± 24	40.6 ± 3.4	9.7 ± 0.2	0.04	0.40	core
2	7.2 ± 1.1	18.7 ± 1.3	475 ± 78	21.6 ± 3.7	3.9 ± 0.3	0.10	0.53	
3	5.1 ± 0.4	12.2 ± 0.5	450 ± 40	10.1 ± 1.0	16.0 ± 0.7	0.11	0.64	
4	6.0 ± 0.6	21.5 ± 1.0	361 ± 38	20.7 ± 2.3	7.0 ± 0.3	0.00	0.49	
5	2.7 ± 1.0	1.5 ± 0.4	963 ± 379	0.7 ± 0.3	37.6 ± 9.0	0.81	2.71	filament?
6	4.5 ± 0.7	4.5 ± 0.4	772 ± 119	3.2 ± 0.5	27.7 ± 2.2	0.51	1.11	outskirts

Table 7. Properties of main regions of RXCJ0232.2–4420.

N	kT keV	ρ_e 10^{-4} cm^{-3}	S keV cm^2	P, 10^{-12} ergs cm^{-3}	$M_{\rm gas}$ $10^{12} M_\odot$	$r_{\min}$ Mpc	$r_{\max}$ Mpc	Remarks
1	8.9 ± 2.6	34.8 ± 4.3	388 ± 119	49.8 ± 15.9	1.1 ± 0.1	0.21	0.36	
2	8.0 ± 1.2	42.1 ± 3.0	305 ± 50	53.7 ± 9.2	1.3 ± 0.1	0.16	0.29	
3	5.1 ± 0.2	169.0 ± 4.3	77 ± 4	136.9 ± 7.3	1.7 ± 0.0	0.00	0.10	cool core
4	7.6 ± 0.5	54.3 ± 1.3	245 ± 17	65.9 ± 4.7	5.7 ± 0.1	0.08	0.32	
5	8.5 ± 2.0	51.3 ± 4.8	287 ± 68	70.1 ± 17.4	0.8 ± 0.1	0.15	0.24	
6	6.3 ± 1.0	40.1 ± 3.2	248 ± 43	40.3 ± 7.4	2.0 ± 0.2	0.14	0.36	
7	7.9 ± 2.6	12.6 ± 1.7	677 ± 235	15.9 ± 5.7	3.6 ± 0.5	0.43	0.79	
8	6.5 ± 0.4	12.7 ± 0.3	557 ± 39	13.3 ± 1.0	24.5 ± 0.6	0.24	0.76	
9	5.0 ± 0.7	19.8 ± 1.5	315 ± 46	15.7 ± 2.4	4.2 ± 0.3	0.19	0.53	entropy tail
10	6.9 ± 2.7	$39.8 \pm 11.$	275 ± 118	44.0 ± 21.3	0.8 ± 0.2	0.18	0.35	
11	8.9 ± 2.8	4.4 ± 0.3	1532 ± 494	6.4 ± 2.1	17.7 ± 1.3	0.57	1.27	forward shock
12	3.1 ± 0.5	5.6 ± 0.7	448 ± 83	2.8 ± 0.6	10.0 ± 1.3	0.48	1.11	outskirts
13	8.3 ± 4.3	4.5 ± 0.9	1405 ± 749	6.0 ± 3.3	5.7 ± 1.2	0.52	1.12	

Table 8. Properties of main regions of RXCJ0307.0–2840.

N	kT keV	ρ_e 10^{-4} cm^{-3}	S keV cm^2	P, 10^{-12} ergs cm^{-3}	$M_{\rm gas}$ $10^{12} M_\odot$	$r_{\min}$ Mpc	$r_{\max}$ Mpc	Remarks
1	6.3 ± 1.2	85.9 ± 12.2	151 ± 31	87.4 ± 20.3	0.3 ± 0.0	0.07	0.14	
2	6.1 ± 1.6	72.2 ± 12.9	163 ± 47	70.4 ± 22.3	0.2 ± 0.0	0.09	0.16	
3	5.5 ± 0.3	64.7 ± 1.6	157 ± 10	56.6 ± 3.8	4.1 ± 0.1	0.02	0.22	
4	4.3 ± 0.3	157.7 ± 8.6	68 ± 5	108.5 ± 9.2	0.6 ± 0.0	0.00	0.09	cool core
5	6.8 ± 0.7	21.3 ± 1.2	408 ± 46	23.1 ± 2.8	2.7 ± 0.2	0.17	0.43	
6	5.7 ± 0.8	25.2 ± 1.9	307 ± 45	22.9 ± 3.6	2.1 ± 0.2	0.19	0.43	
7	6.4 ± 1.3	28.6 ± 2.2	318 ± 66	29.5 ± 6.4	1.4 ± 0.1	0.17	0.35	
8	5.9 ± 0.5	14.3 ± 0.4	465 ± 37	13.6 ± 1.1	14.1 ± 0.4	0.16	0.68	
9	4.7 ± 0.5	4.4 ± 0.2	808 ± 83	3.3 ± 0.3	44.5 ± 1.8	0.31	1.17	

(region 9). However, the low-entropy zone exhibits a pressure typical for its distance to the center. The indicated pressure and entropy fluctuations are rather marginal, ∼ 2 sigma. The strong fluctuations in both entropy and pressure, reported in Tab.4 are entirely due to the presence of the filament.

3.7. RXCJ1131.9–1955 ("whirlpool", A1300)

The most remarkable feature of this cluster is an unusually elongated pressure map. We have cast the name "whirlpool" cluster for this object due to the observed propeller-like temperature structure. Three temperature rims are observed to be filled with colder blobs. In the pressure this makes some small-scale structure, while on large-scales the structure is seen mainly in the entropy map. There is a parcel of low entropy gas at the center of the southern part of the cluster.

On the largest scale, there is an elongation towards the north, practically in all the maps in the direction where we also see the second largest galaxy concentration in the optical (Böhringer et al. 2002). This is probably due to the response of the gas pressure to the joint potential well of the two clusters that make up A1300. There is a central E-W ridge of high temperature, that may reflect the compression of the central region due to the approximately N–S merge of the cluster.

The spectroscopic analysis is reported in Table 11 and Fig.11. The cluster has a complex temperature structure in the core, which we assign to the distorted cool core, which partially preserves both the low entropy and high pressure. Also the temperature decreases strongly towards cluster outskirts. The large scatter in the entropy profile is most probably due to the contribution of the substructure, associated with the second optical component. The outmost bin has an entropy strongly deviating from the scaling. The analysis confirms the statistical sig-
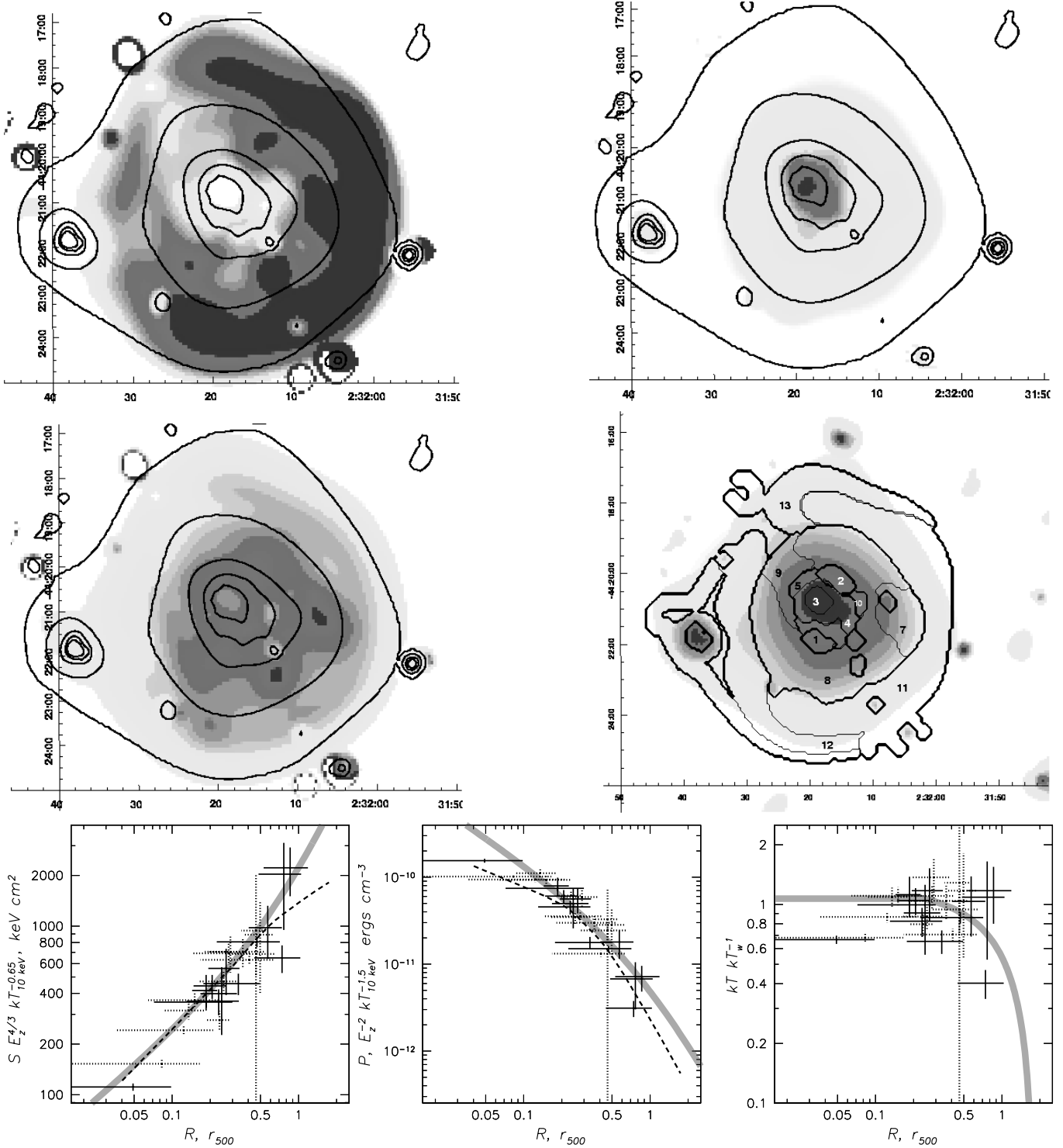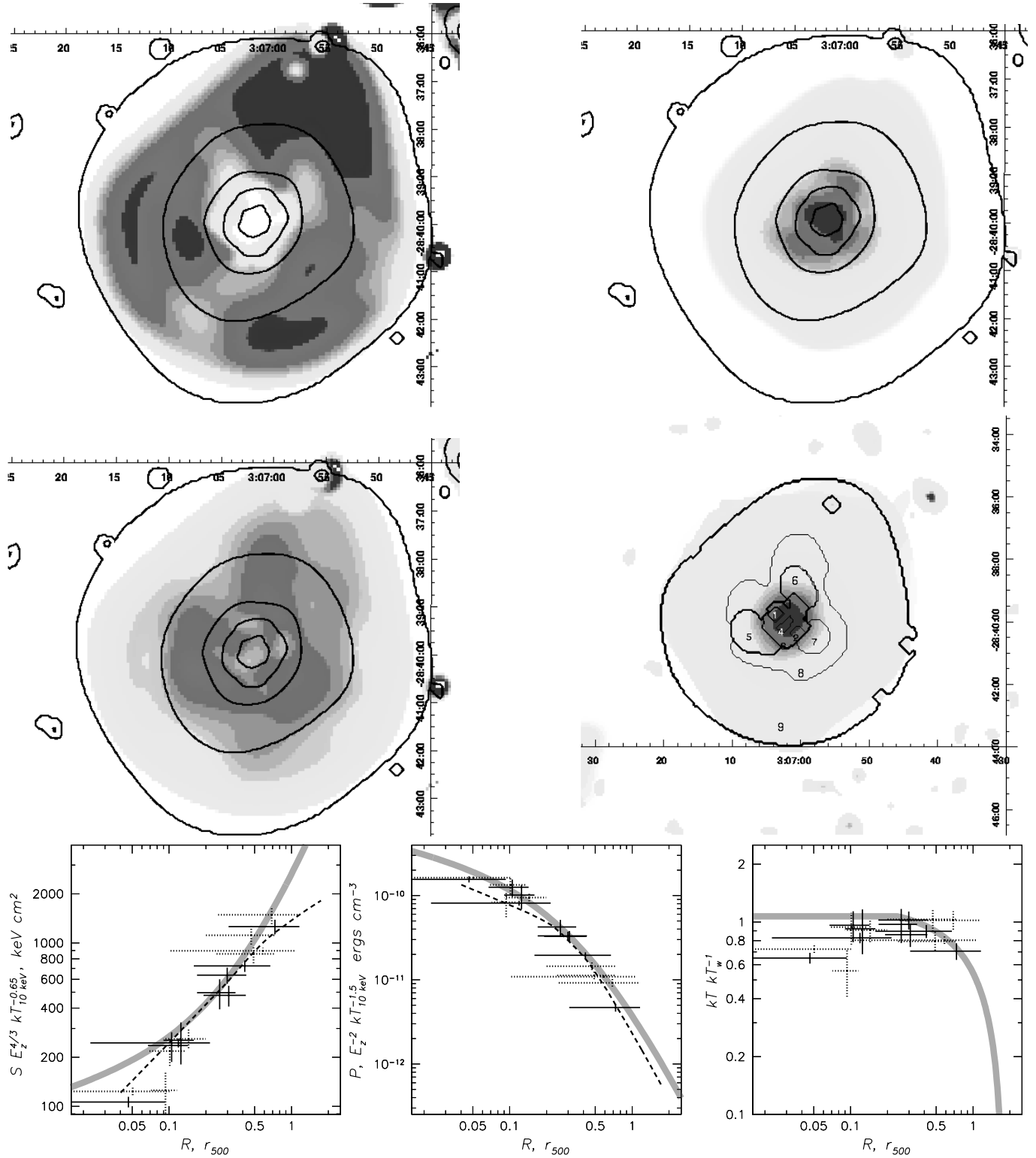
Fig. 7. RXCJ0232.2–4420. Figure caption is similar to that of Fig.5. The surface brightness image is overlaid with contours showing the spectral extraction regions with numbers corresponding to those in Table 7.

nificance of the low entropy blobs in the south and reveals a pressure enhancement in the north. Combining these two features together, a plausible interpretation is that the subcluster has lost its gas on approaching the cluster from the south and is currently located north to the main cluster.

3.8. RXCJ2337.6+0016

The image shows an East-West elongated core on the small scale, while on the large scale it appears to be symmetric. The pressure map has two maxima and two elongations towards the south-west and south-east. There are some ring-like structures in the temperature map. The entropy state of the cluster ICM appears to correspond to the late stage of a core disruption with
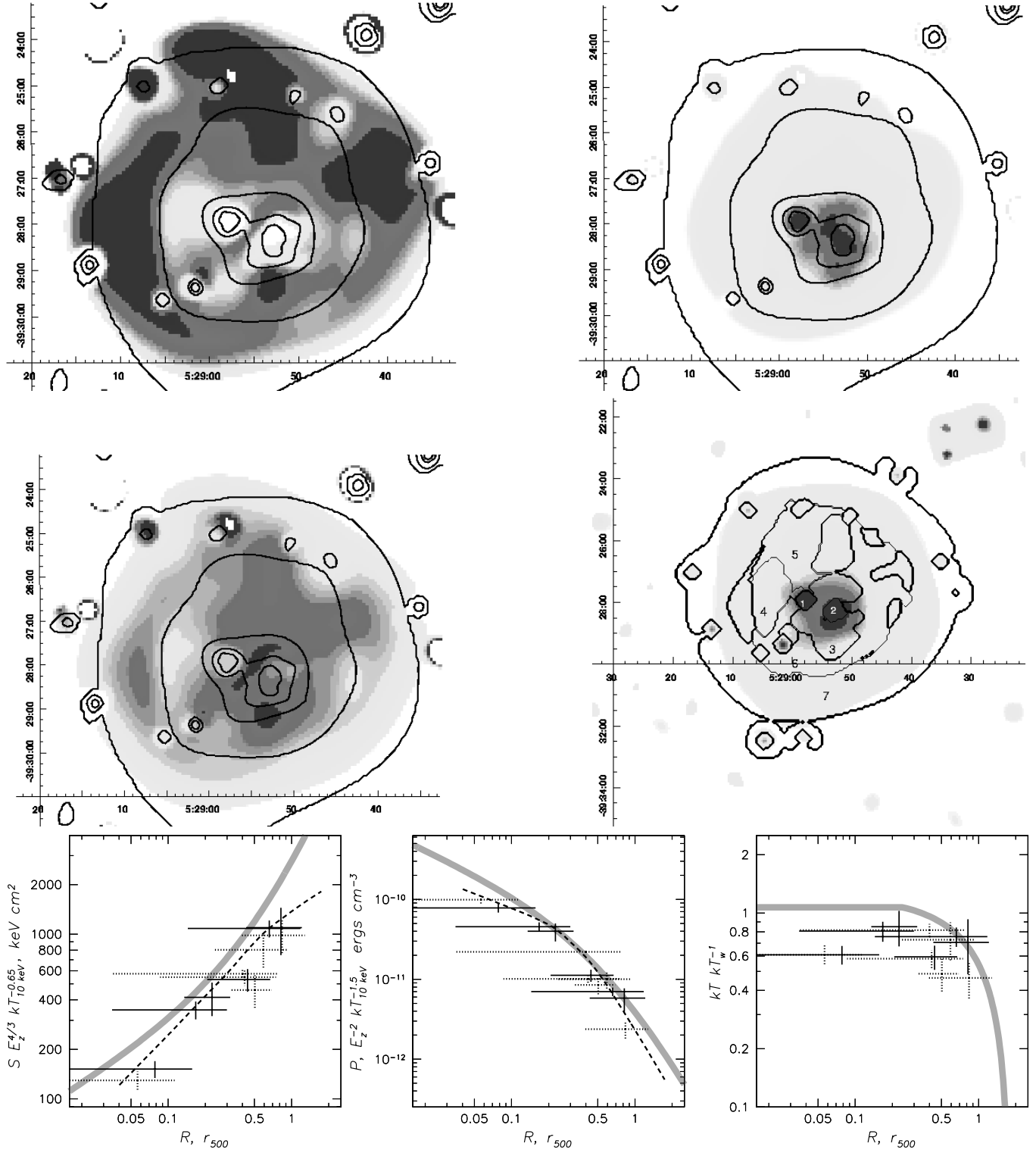
Fig. 8. RXCJ0307.0–2840. Figure caption is similar to that of Fig.5. The surface brightness image is overlaid with contours showing the spectral extraction regions with numbers corresponding to those in Table 8.

filaments of the low-entropy gas spread over a large volume. The position of the entropy minimum is offset from the peak in the pressure.

The cluster has a clover leaf structure in the entropy map like the 0532.9–3701. Two pressure maxima could indicate the

core rebounce. The symmetry in the pressure map is regained at 1.5 arcminute radius.

The spectroscopic analysis is reported in Table 12 and Fig.12. The scenario of the disrupted core (region 4) is sup-

Fig. 9. RXCJ0528.9–3927. Figure caption is similar to that of Fig.5. The surface brightness image is overlaid with contours showing the spectral extraction regions with numbers corresponding to those in Table 9.

ported by the spectral analysis (see also Fig.14). The pressure enhancement (region 5) is marginal.

3.9. RXCJ0658–5557 (the "bullet" cluster)

Famous for its Chandra image (Markevitch et al. 2002), the bullet cluster has some distinct features, which also allow us to understand the observation of other clusters. With a Mach number of 3, deduced from the shape of the bullet itself (angle of

Table 9. Properties of main regions of RXCJ0528.9–3927 (the region 1 turned to be a QSO and is omitted).

N	kT keV	ρ_e 10^{-4} cm^{-3}	S keV cm^2	P, 10^{-12} ergs cm^{-3}	M_{gas} $10^{12} M_\odot$	r_{min} Mpc	r_{max} Mpc	Remarks
2	4.7 ± 0.5	93.8 ± 6.0	106 ± 12	70.6 ± 9.0	2.0 ± 0.1	0.00	0.17	core region
3	6.2 ± 0.7	41.2 ± 2.5	242 ± 30	41.1 ± 5.4	6.1 ± 0.4	0.04	0.32	
4	6.5 ± 1.4	34.3 ± 5.0	288 ± 66	35.9 ± 9.1	2.1 ± 0.3	0.15	0.34	
5	5.4 ± 1.7	6.0 ± 0.4	764 ± 244	5.2 ± 1.7	9.1 ± 0.7	0.46	1.31	
6	4.6 ± 0.7	13.8 ± 1.4	370 ± 58	10.1 ± 1.8	10.2 ± 1.0	0.22	0.72	
7	5.8 ± 0.7	6.8 ± 0.3	755 ± 89	6.3 ± 0.8	54.6 ± 2.1	0.16	1.27	

Table 10. Properties of main regions of RXCJ0532.9–3701.

N	kT keV	ρ_e 10^{-4} cm^{-3}	S keV cm^2	P, 10^{-12} ergs cm^{-3}	M_{gas} $10^{12} M_\odot$	r_{min} Mpc	r_{max} Mpc	Remarks
1	6.0 ± 1.1	36.0 ± 3.9	256 ± 52	34.6 ± 7.6	1.1 ± 0.1	0.13	0.31	
2	11.6 ± 2.9	39.7 ± 3.1	461 ± 118	73.6 ± 19.3	2.0 ± 0.2	0.12	0.31	
3	8.6 ± 3.2	48.9 ± 5.3	300 ± 112	67.7 ± 25.8	1.4 ± 0.1	0.09	0.24	
4	6.5 ± 0.9	31.1 ± 1.8	307 ± 43	32.6 ± 4.8	2.4 ± 0.1	0.10	0.36	
5	6.7 ± 0.5	43.0 ± 1.2	253 ± 18	46.1 ± 3.4	5.9 ± 0.2	0.00	0.36	core
6	6.9 ± 0.7	47.6 ± 2.0	243 ± 27	52.5 ± 6.1	2.9 ± 0.1	0.02	0.37	
7	7.3 ± 1.7	30.4 ± 3.0	349 ± 84	35.6 ± 9.0	2.3 ± 0.2	0.20	0.37	
8	1.4 ± 0.3	3.3 ± 0.6	286 ± 65	0.7 ± 0.2	17.0 ± 3.2	0.84	1.71	filament
9	4.5 ± 0.4	5.6 ± 0.2	665 ± 55	4.1 ± 0.4	57.0 ± 1.7	0.30	1.15	

Table 11. Properties of main regions of RXCJ1131.9–1955.

N	kT keV	ρ_e 10^{-4} cm^{-3}	S keV cm^2	P, 10^{-12} ergs cm^{-3}	M_{gas} $10^{12} M_\odot$	r_{min} Mpc	r_{max} Mpc	Remarks
1	8.5 ± 0.6	32.4 ± 0.8	387 ± 28	43.9 ± 3.2	9.4 ± 0.2	0.03	0.39	
2	7.4 ± 1.3	29.1 ± 1.8	363 ± 64	34.5 ± 6.3	2.3 ± 0.1	0.21	0.41	
3	5.1 ± 0.5	33.2 ± 2.9	231 ± 27	27.3 ± 3.6	1.6 ± 0.1	0.15	0.38	
4	5.5 ± 0.8	45.2 ± 4.0	201 ± 33	39.7 ± 7.0	1.4 ± 0.1	0.14	0.31	
5	6.0 ± 0.4	79.1 ± 2.5	151 ± 11	76.0 ± 5.9	2.3 ± 0.1	0.02	0.19	
6	2.1 ± 0.4	2.7 ± 0.5	503 ± 107	0.9 ± 0.2	34.7 ± 5.9	0.89	1.95	
7	4.5 ± 0.5	4.3 ± 0.2	797 ± 89	3.1 ± 0.4	58.5 ± 2.6	0.39	1.59	
8	6.9 ± 0.8	10.1 ± 0.3	680 ± 81	11.2 ± 1.3	20.6 ± 0.6	0.29	0.98	
9	10.6 ± 2.0	13.3 ± 0.6	875 ± 169	22.7 ± 4.4	4.7 ± 0.2	0.35	0.79	
10	8.0 ± 1.4	15.5 ± 1.3	599 ± 111	19.9 ± 3.9	3.5 ± 0.3	0.25	0.55	

the Mach cone), the subcluster makes an entropy enhancement in front of it. There are two other large entropy peaks behind and to the south from the bullet. Apart from the small-scale structure in the center, there appears to be a lack of features on the pressure map, which we attribute to the propagation of the shock out to large radii, thus strongly reducing the contrast. Therefore, the bullet indicates a situation of a strong merger that is just completed in the center and now moves to outskirts. The entropy structure of the core of the main cluster appears disrupted, yet the minimum is retained, while becoming shallow. In the temperature map we see clear signatures of turbulence, as indicated by the stochastic fluctuations, which in other clusters correspond to a late stage of merging. This once again demonstrates that the time scales for the relaxation are very different for the cluster center and outskirts. On the largest scale the pressure as well as the image appears to be quite smooth.

A weak lensing mass reconstruction of Clowe et al. (2003) shows that the cluster exhibits three dark matter peaks, with only the weakest of them corresponding to an X-ray peak, yet all of them are preceded by a shocked zone, seen in the entropy map. The main pressure peak is approximately located at the position of the center of the mass distribution from the weak lensing reconstruction. This center is adopted for the volume calculations and reported in Table 1. The entropy dip of the bullet is offset from the potential minimum and there is no entropy dip associated with the potential minimum of the main cluster. There are, however, entropy fluctuations in the pressure core, possibly associated with debris of the entropy core of the main cluster.

The spectroscopic analysis is reported in Table 13 and Fig.13. It reveals temperature fluctuations by a factor of 1.5. The temperature of the bullet is only slightly lower than the bulk of the cluster. However it exhibits a distinctly low entropy, which also allows us to trace the tail of the bullet. The zone assigned to bullet can be seen as negative deviation in entropy profile in Fig.13. The bullet pressure peak is confirmed; it amounts to 20% and is located behind the zone of lowest entropy in the bullet.
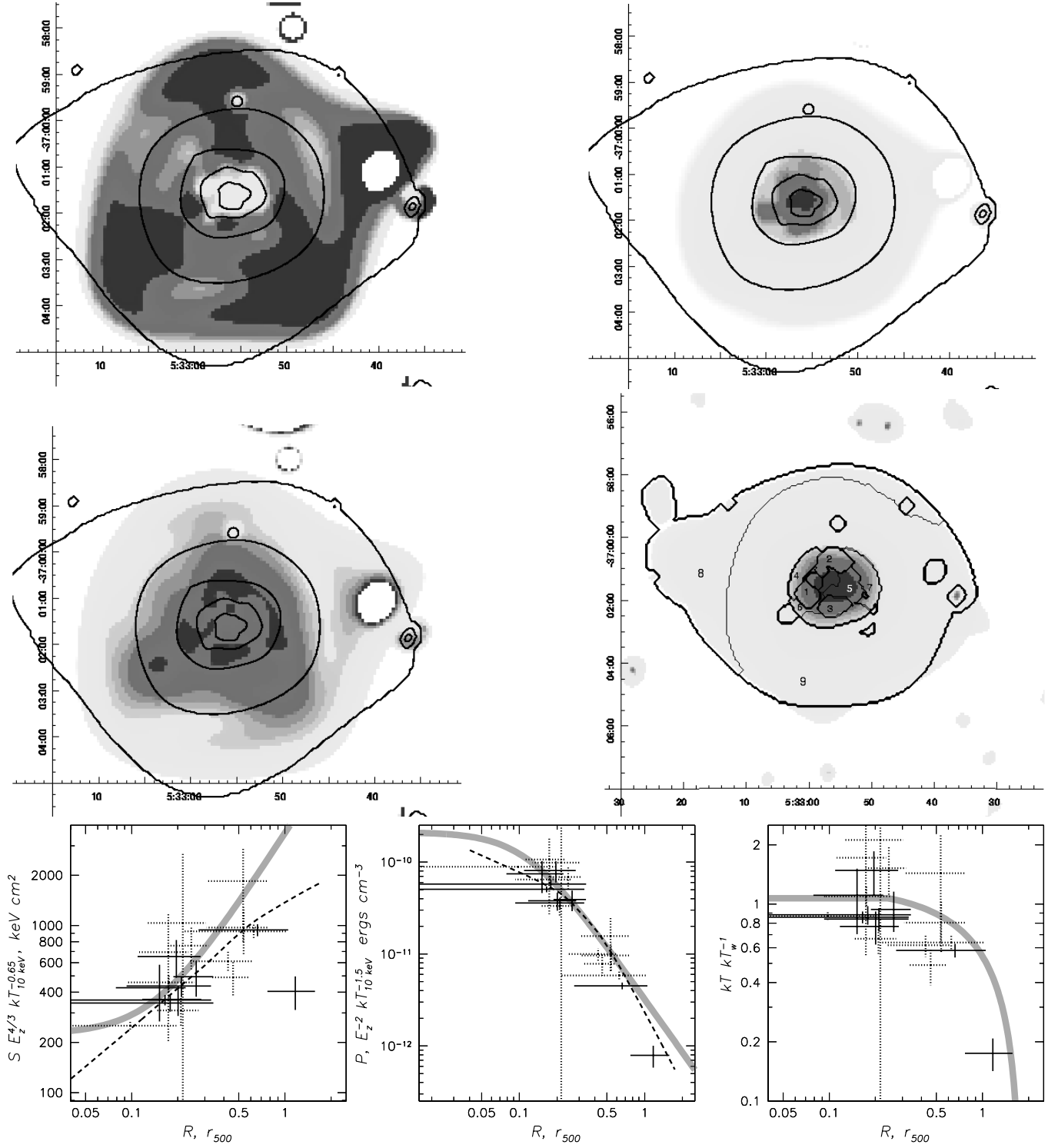
Fig. 10. RXCJ0532.9–3701. Figure caption is similar to that of Fig.5. The surface brightness image is overlaid with contours showing the spectral extraction regions with numbers corresponding to those in Table 10.

By combining together all the high-entropy zones, associated with the shock heating, we have achieved 99% significance in the temperature variation, from 10. to 14 ± 2 keV. This corresponds to a Mach number of 1.4 ± 0.2. This estimate is lower, compared to the shock parameters deduced from the image showing the Mach cone. A higher Mach number would be obtained from the entropy enhancement: 2.6 ± 0.2. It is plau-

sible that the extraction region captures both shock and post-shock gas. The later has lower pressure, but records its state in the entropy. As was noted above, the observed shock is located in front of the outward moving dark matter potential. Since the potentials carry no longer any gas, they do not cause this shock, but just travel at the same speed. This implies that we observe the initial forward shock propagating through the cluster.
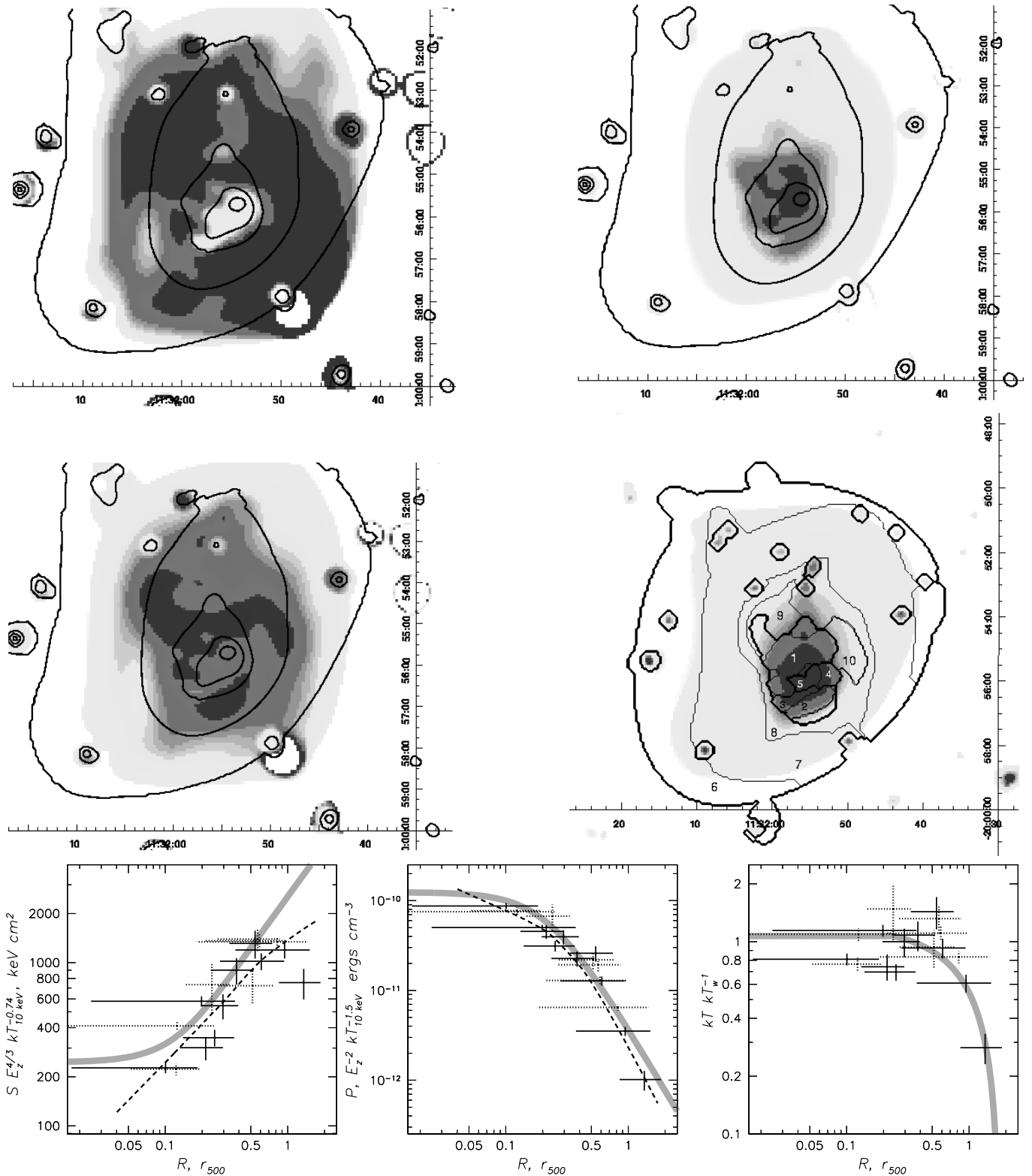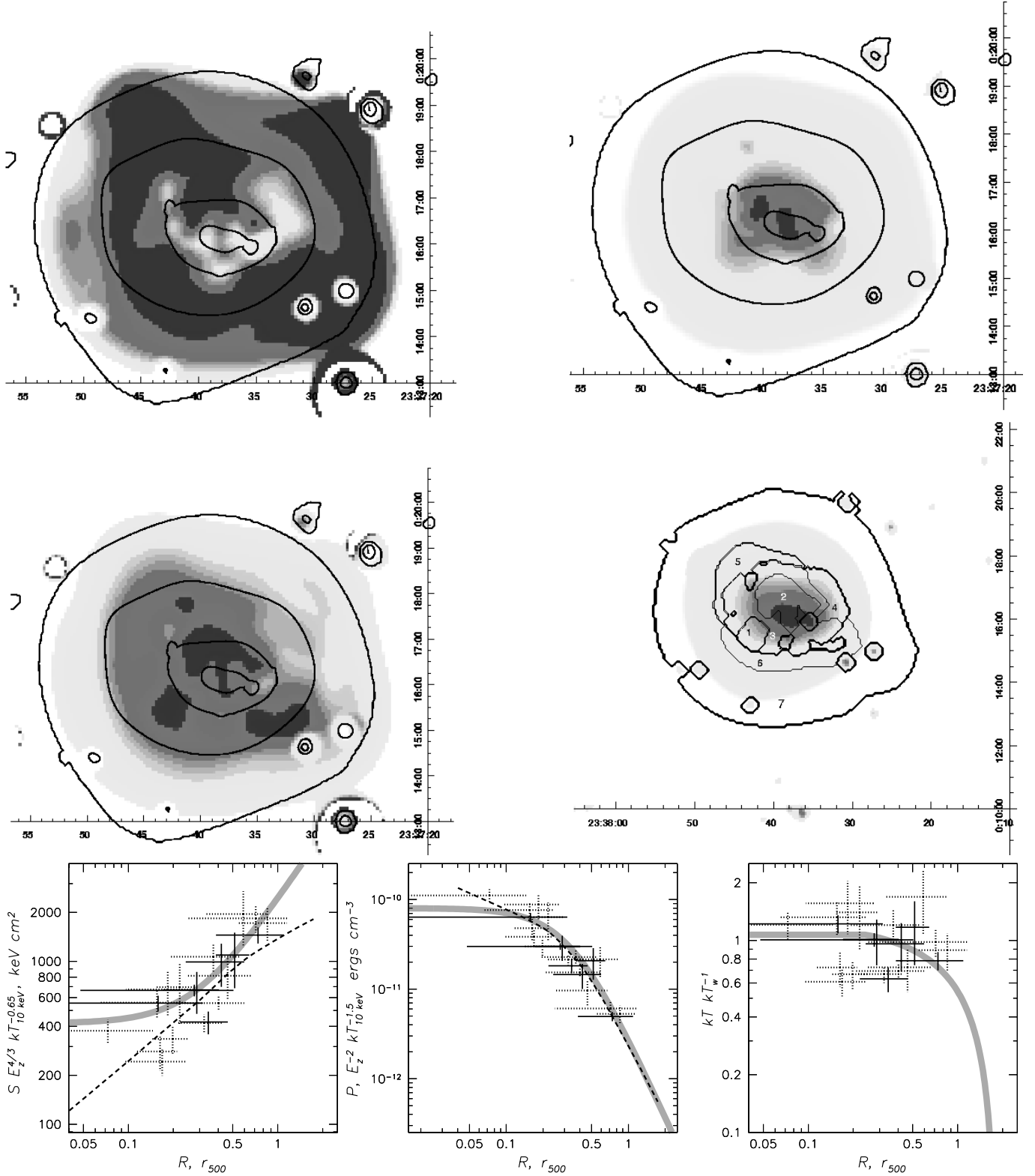
Fig. 11. RXCJ1131.9–1955. The figure caption is similar to that of Fig.5. The surface brightness image is overlaid with contours showing the spectral extraction regions with numbers corresponding to those in Table 11.

The entropy ratio also shows that the eastern part of the cluster has lower entropy, as due to the stripping of the bulk of the bullet cluster.

4. Discussion and Summary

An analysis of the two-dimensional structure in the REFLEX clusters, as seen in the images and spectral hardness ratio maps, reveals statistically significant substructure, probably originat-

Fig. 12. RXCJ2337.6+0016. The figure caption is similar to that of Fig.5. The surface brightness image is overlaid with contours showing the spectral extraction regions with numbers corresponding to those in Table 12.

ing from different stages of cluster merger. We are able to see the substructure even at very late merger stages, where for example the X-ray image appears to be quite symmetric. We identify the entropy to be most sensitive to both late stage mergers with the associated slow buoyancy action of relaxation of the cluster and to strong shocks, which change the entropy. Two mergers with large Mach numbers are found.

Table 12. Properties of main regions of RXCJ2337.6+0016.

N	kT keV	ρ_e 10^{-4} cm^{-3}	S keV cm^2	P, 10^{-12} ergs cm^{-3}	M_{gas} $10^{12} M_\odot$	r_{min} Mpc	r_{max} Mpc	Remarks
1	7.6 ± 2.0	21.3 ± 3.4	460 ± 133	25.9 ± 8.1	1.5 ± 0.2	0.18	0.43	
2	9.2 ± 1.0	37.3 ± 1.1	381 ± 42	54.7 ± 6.2	6.0 ± 0.2	0.00	0.34	
3	7.6 ± 0.6	21.3 ± 0.5	456 ± 38	25.9 ± 2.2	13.0 ± 0.3	0.05	0.54	
4	4.7 ± 0.7	20.7 ± 1.9	292 ± 47	15.7 ± 2.7	2.9 ± 0.3	0.24	0.50	disrupted core
5	8.8 ± 3.2	12.7 ± 1.5	751 ± 281	17.8 ± 6.9	3.5 ± 0.4	0.41	0.69	secondary pressure peak?
6	7.2 ± 2.0	10.9 ± 1.4	681 ± 202	12.5 ± 3.9	4.0 ± 0.5	0.26	0.64	
7	5.9 ± 0.6	4.5 ± 0.2	997 ± 113	4.3 ± 0.5	41.2 ± 1.8	0.41	1.17	

Table 13. Properties of main regions of RXCJ0658–5557.

N	kT keV	ρ_e 10^{-4} cm^{-3}	S keV cm^2	P, 10^{-12} ergs cm^{-3}	M_{gas} $10^{12} M_\odot$	r_{min} Mpc	r_{max} Mpc	Remarks
1	12.1 ± 1.0	85.2 ± 1.9	290 ± 26	165.3 ± 14.8	2.7 ± 0.1	0.00	0.22	P core-1
2	14.0 ± 1.8	10.8 ± 0.3	1332 ± 169	24.3 ± 3.1	18.6 ± 0.5	0.45	1.12	shock
3	10.4 ± 0.6	21.3 ± 0.3	626 ± 35	35.3 ± 2.0	20.6 ± 0.3	0.14	0.63	tail
4	8.7 ± 1.0	4.0 ± 0.1	1593 ± 190	5.6 ± 0.7	59.6 ± 1.5	0.61	1.79	main-2
5	12.2 ± 0.9	34.2 ± 0.6	540 ± 42	67.1 ± 5.3	8.8 ± 0.2	0.24	0.58	P core-3
6	9.4 ± 0.7	43.1 ± 0.9	354 ± 27	64.6 ± 5.0	4.4 ± 0.1	0.11	0.45	bullet tail N
7	9.9 ± 0.6	64.3 ± 1.1	286 ± 17	101.8 ± 6.2	4.0 ± 0.1	0.11	0.32	bullet tail W
8	11.4 ± 1.0	51.0 ± 1.0	383 ± 33	92.9 ± 8.0	5.1 ± 0.1	0.07	0.39	P core-2
9	10.0 ± 0.5	12.2 ± 0.2	871 ± 48	19.5 ± 1.1	42.0 ± 0.6	0.30	1.13	main-1
10	8.0 ± 0.6	64.7 ± 1.9	230 ± 17	82.5 ± 6.5	1.6 ± 0.0	0.27	0.43	bullet peak
11	7.7 ± 0.5	45.8 ± 0.9	281 ± 17	56.9 ± 3.5	4.1 ± 0.1	0.25	0.52	bullet front

A statistical analysis of the substructure in the pressure and entropy maps, reveals significant fluctuations around the mean profile. Typically, pressure fluctuations are found on the 30% level, while the entropy fluctuations are at the 20% level. Apparently, smoother appearance of the pressure maps should be attributed to the larger dynamical range of the map, covering typically two orders of magnitude. A comparison of our sample with a similar analysis of hydro-dynamical simulations by Finoguenov et al. (2005) reveals a similar distribution of clusters vs the level of the substructure in both entropy and pressure.

A number of clusters exhibit a presence of low entropy gas in the outskirts, deviating by at least an order of magnitude from the prescription of gravitational heating. Surprisingly enough, these regions have gas pressures similar to that of the cluster at a similar distance from the center. This argues in favor of these regions being embedded in the cluster gas and maintaining the pressure equilibrium, therefore revealing a medium survived from the accretion shock heating. Existence of this effect has been suggested by the simulations (e.g. Motl et al. 2004), but has so far only been reported for A85 (Durret et al. 2005).

Incomplete (in a sense of being on-going) shock propagation in clusters soon after the major merging event could also be a cause of the low entropies seen at the outskirts. In fact, the clusters in the advanced stage of interaction have systematically higher entropy at r_{500} compared to the average trend.

References

Belsole, E., Sauvageot, J.-L., Pratt, G. W., & Bourdin, H. 2005, A&A, 430, 385

Böhringer, H., et al. 2001, A&A, 369, 826

Böhringer et al. 2002, Mesenger

Briel, U. G., Finoguenov, A., & Henry, J. P. 2004, A&A, 426, 1

Churazov, E., Gilfanov, M., Forman, W., & Jones, C. 1999, ApJ, 520, 105

Clowe, D., Gonzalez, A., & Markevitch, M. 2004, ApJ, 604, 596

De Luca, A., & Molendi, S. 2004, A&A, 419, 837

Durret, F., Lima Neto, G. B., & Forman, W. 2005, A&A, 432, 809

Finoguenov, A., Reiprich, T. H., & Böhringer, H. 2001, A&A, 368, 749

Finoguenov, A., Mohr, J. J., Bialek, J. J., Evrard, A., Sanderson, A. J. R. 2005 ApJ, subm.

Jones, C., & Forman, W. 1984, ApJ, 276, 38

Henry, J. P., Finoguenov, A., & Briel, U. G. 2004, ApJ, 615, 181

Kempner, J. C., & David, L. P. 2004, MNRAS, 349, 385

Markevitch, M., et al. 2002, ApJ, 567, 27

Mahdavi, A., Finoguenov, A., Böhringer, H., Geller, M. J., & Henry, J. P. 2005, ApJ, 622, 187

Motl, P. M., Burns, J. O., Loken, C., Norman, M. L., & Bryan, G. 2004, ApJ, 606, 635
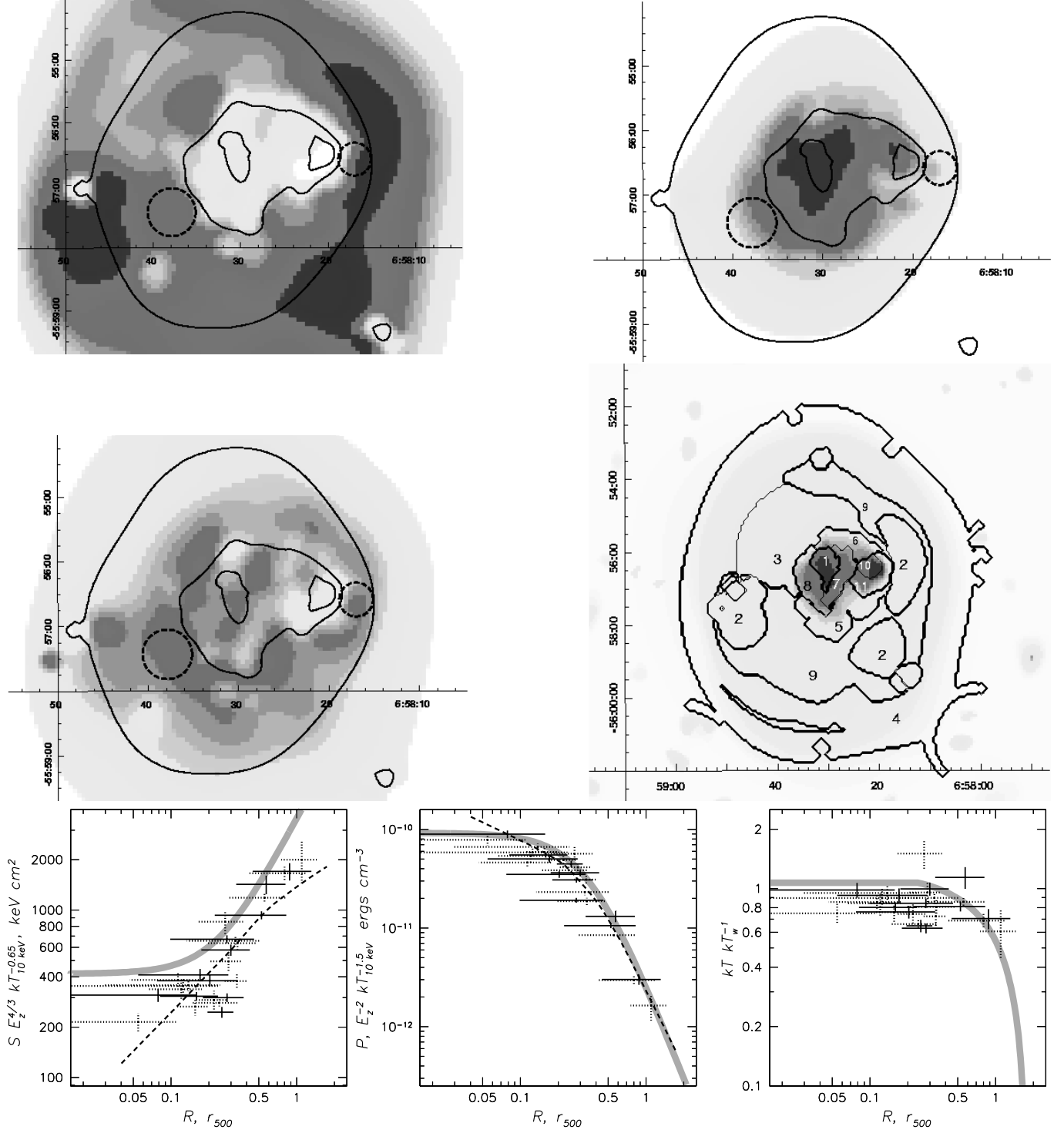
Fig. 13. RXCJ0658–5557. Figure caption is similar to that of Fig.5. The surface brightness image is overlaid with contours showing the spectral extraction regions with numbers corresponding to those in Table 13. Two dashed line circles indicate the positions of the two peaks reveals in the weak lensing analysis of Clowe et al. (2004)

Ponman, T. J., Sanderson, A. J. R., Finoguenov, A. 2003, MNRAS, 343, 331

Randall, S. W., Sarazin, C. L., & Ricker, P. M. 2002, ApJ, 577, 579

Reiprich, T. H., Sarazin, C. L., Kempner, J. C., & Tittley, E. 2004, ApJ, 608, 179

Rowley, D. R., Thomas, P. A., & Kay, S. T. 2004, MNRAS, 352, 508

Sanderson, A. J. R., Finoguenov, A., Mohr, J.J. 2005, ApJ, in press (astro-ph/0412316)

Vikhlinin, A., et al. 1998, ApJ, 502, 558

Vikhlinin, A., Markevitch, M., Murray, S. S., Jones, C., Forman, W., & Van Speybroeck, L. 2005, ApJ, in press, (astro-ph/0412306)

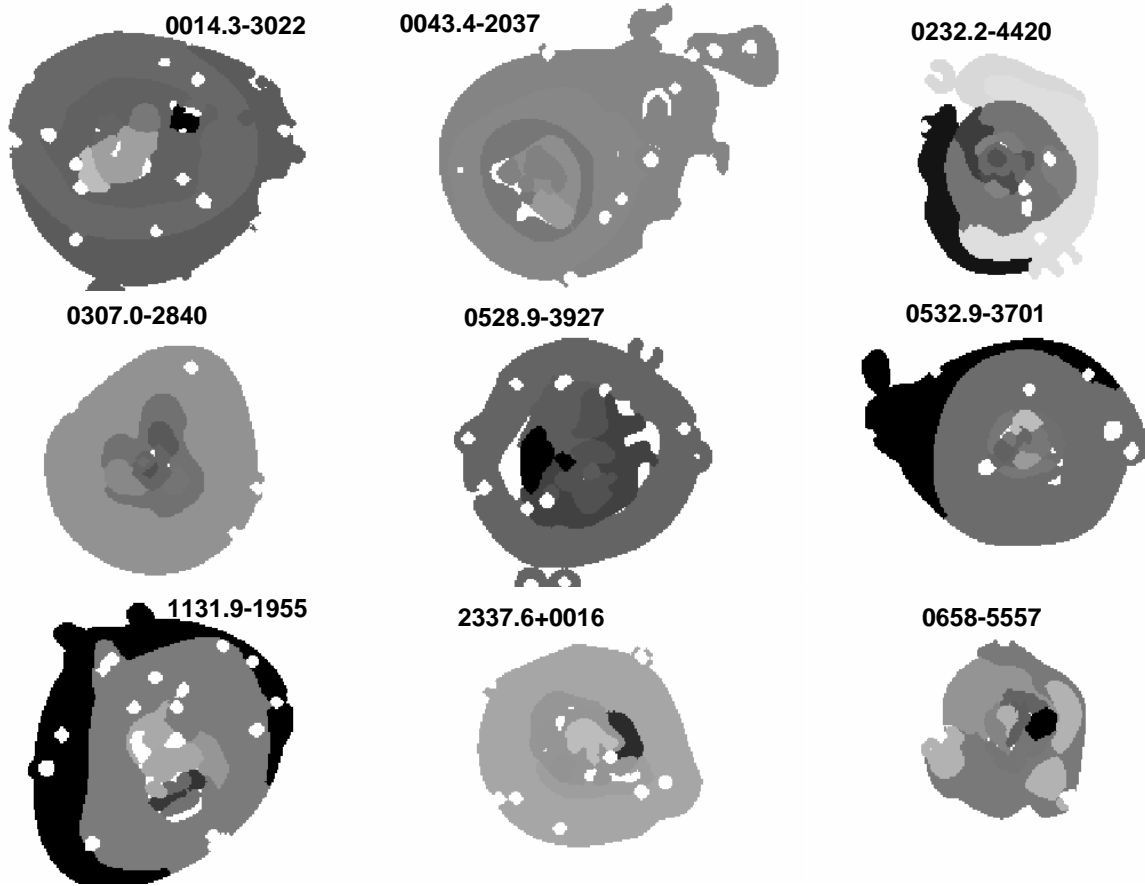Voit, G. M., & Bryan, G. L. 2001, Nature, 414, 425

Voit G. M., 2005, RvMP, 77, 207

Fig. 14. Maps of the ratio between the observed entropy and the average trends measured in the DXL sample. The different shades of grey stand for a different value of the ratio, light – 1.9 (seen only in RXCJ 0232.2-4420 cluster), grey – 1.1 (a dominant color of both RXCJ 0043.4-2037 and RXCJ 0307.0-2840 clusters), dark grey – 0.9 (a dominant color of RXCJ 0014.3-3022), black – 0.4 (e.g. tail of RXCJ 0532.9-3701).

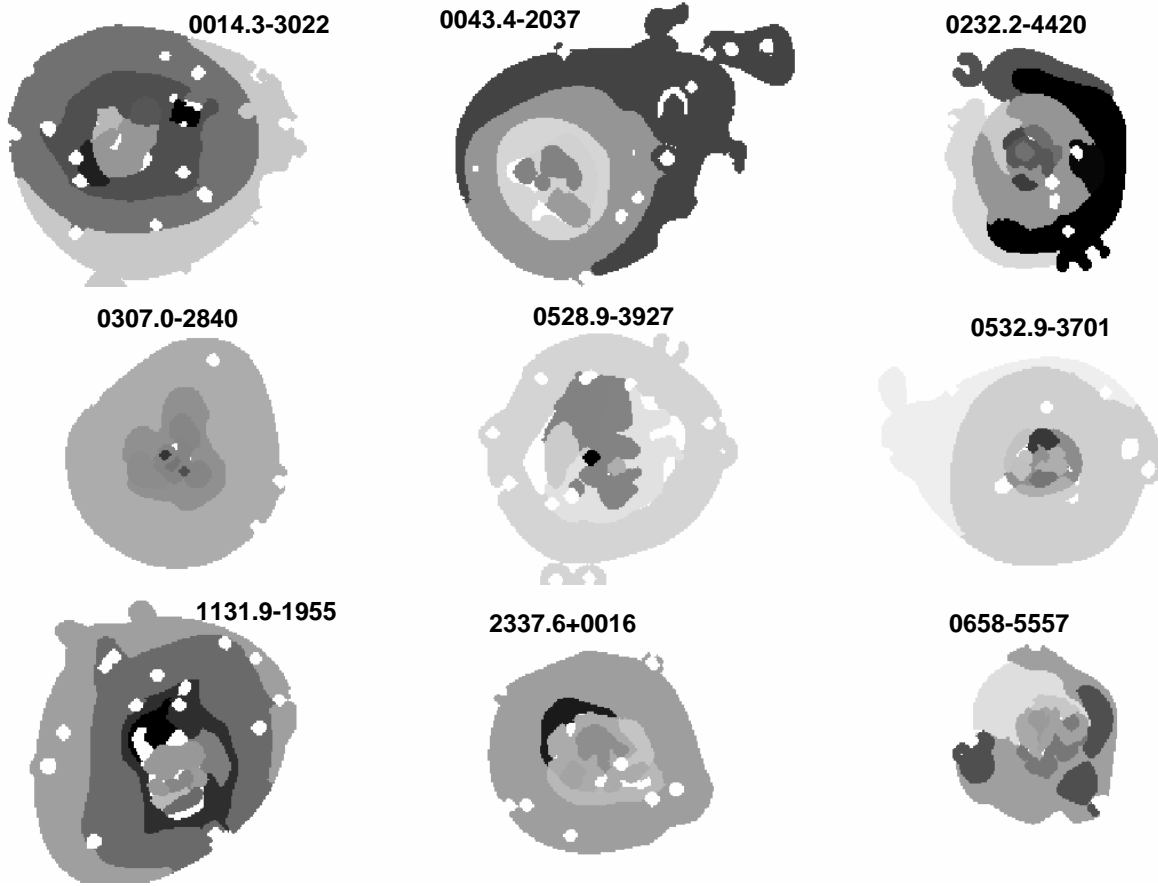Zhang Y.-Y., et al. 2004, A&A, 413, 49
Zhang Y.-Y., et al. 2005, A&A, subm.

Fig. 15. Maps of the ratio between between the observed pressure and the average trends measured in the DXL sample. The different shades of grey stand for a different value of the ratio, light – 0.5 (e.g. tail of RXCJ 0532.9-3701), grey – 1.1 (a dominant color of RXCJ 0532.9-3701), dark grey – 1.4 (a tail of RXCJ 0043.4-2037), black – > 2.